Coalescence of Two Equal-sized Deformable Drops in an Axisymmetric Flow

Yosang Yoon[1], Fabio Baldessari[1], Hector. D. Ceniceros[2], and L. Gary Leal[3]

[1]Department of Chemical Engineering, University of California at Santa Barbara, Santa Barbara, CA 93106-5080, USA
[2]Department of Mathematics, University of California at Santa Barbara, Santa Barbara, CA 93106-5080, USA
[3] Department of Chemical Engineering and Department of Materials, University of California at Santa Barbara, Santa Barbara, CA 93106-5080, USA

Abstract

The coalescence of two equal-sized deformable drops in an axisymmetric flow is studied, using a boundary-integral method. An adaptive mesh refinement method is used to resolve the local small-scale dynamics in the gap and to retain a reasonable speed of computation. The thin film dynamics is successfully simulated, with sufficient stability and accuracy, up to a film thickness of $O(10^{-4})$ times the undeformed drop radius, for a range of capillary numbers, Ca, from $O(10^{-4}-10^{-1})$ and viscosity ratios from $O(0.1-10)$. The results are compared with experimental results from our earlier studies as well as the simple scaling theory for film drainage. The collisions for time-independent flow simulating head-on collisions in the experimental studies show two distinctively different regimes. At lower capillary numbers, the interfaces of thin film between the colliding drops remain almost spherical up to the point of film rupture, and the dimensionless drainage time scales as $t_d G \sim Ca$. At higher capillary numbers, the film becomes dimpled at an early stage of the collision process, and the rate of the film drainage significantly slows down after the dimple was fully formed. In this case, the drainage

time scales approximately as $t_d G \sim Ca^{3/2}$. The simulation, using a Hamaker constant with a fixed value calculated via Lifshitz theory, qualitatively predicts the experimental results for the higher capillary numbers but not for the lower capillary numbers. The critical conditions for head-on collisions are also examined when the internal circulation within the drop, caused by the external flow, arrests the film drainage. Collisions in a time-dependent flow are also examined to simulate glancing collisions. Although the simulations predict many aspects of the experimental results, the results are only quantitatively accurate, in comparison with the experimental data, for the lowest viscosity ratio of 0.19. The interfaces of the thin film locally bulge outward when the drops are being pulled apart due to the suction pressure. This local deformation causes a secondary (or primary for larger offsets) minimum in the film thickness when $Ca > Ca_c$. At the larger offsets, the coalescence angle continuously increases with Ca up to the separation angle ($\theta = 55 - 58^\circ$), for $Ca < Ca_c$. At smaller offsets, however, the local deformation cannot induce film rupture, as is observed in both the glancing and time-dependent flow collision experiments for the higher viscosity ratios.

1. INTRODUCTION

The interaction and motion of drops in a flow has long been the subject of experimental and theoretical studies due to their fundamental importance in a variety of multi-phase flow systems, such as liquid-liquid extraction, emulsification and polymer blending. Studies of the dynamics, deformation and breakup of single drops was pioneered by Taylor [1, 2]. Youngren and Acrivos [3] were the first to use boundary-integral methods for single drops in axisymmetric extensional flows, and they were followed by Rallision and Acrivos [4]. Theoretical and experimental studies on the dynamics and breakup of single drops have a rich history and are well reviewed by Stone [5].

The physics of the interaction and coalescence of two or more drops is more complex than the dynamics of a single drop and more difficult to study, either theoretically or experimentally. Most of the experimental investigations for coalescence have been performed by measuring the evolution of the drop size distribution of an emulsion or blend subjected to steady or transient flow. The trajectories of a pair of drops in both shear [6] and extensional flow [7] were also studied, but coalescence was not observed due to the relatively large sized drops that were used. Recently, however, the coalescence of two equal-sized drops in the size range, diameter < 100 μm, has been investigated using the four-roll mill at the individual drop level of resolution by our group [8-12]. The fluids were polymeric, but Newtonian under the flow conditions relevant to coalescence, and we considered systems both with and without copolymer surfactant. These studies revealed a number of interesting and often unexpected phenomena. However, an intrinsic limitation of these experiments is that one cannot visualize the details of the thin film

region between the drops, and thus, we can only speculate on the mechanisms for many of these phenomena. This is where theory can play an extremely useful role. At the same time, comparisons between experimental data and predicted results for measurable quantities, such as the film drainage time, or the coalescence angle, can provide a check on the accuracy of the underlying physical assumptions in the theory; chief among these, of course, are the continuum approximations in governing equations and boundary conditions that are applied within the thin film, which can become extremely thin before rupture occurs due to van der Waals forces in the case that the two drops coalesce.

There have been numerous theoretical studies focused on numerical simulation of the interactions of drops either in a flow or in buoyancy driven motion, with or without van der Waals forces. For the asymptotic limit of a small capillary number ($Ca \ll 1$), Yiantsios and Davis [13] have investigated the thin film dynamics for buoyancy driven collisions, within a matched asymptotic framework. A number of numerical studies of the local film drainage have been reported, using a similar asymptotic analysis for various types of collisions, with or without surfactants at the interface [14-17]. A recent thin film study by Baldessari and Leal [18], using a slightly modified asymptotic framework, has shown that the small *overall* drop deformation of $O(Ca)$ due to the external flow can play an important role in the film drainage process, especially in the counter-intuitive case when the capillary number is asymptotically small ($Ca \leq O(10^{-3})$). The thin film studies referenced above only considered the local motion within the drops that is driven via coupling with the tangential motion within the thin film. In effect, this assumes that the external flow field affects drop coalescence only via the overall deformation of the drop, which affects the shape and thickness of the thin film, and the hydrodynamic force

that pushes the drops together. However, recently, both a numerical study of the full drop collision problem by Cristini *et al.* [19] and an asymptotic analysis by Nemer *et al*. [20] have shown that the film drainage process can also be affected by the recirculating flow that is induced inside the drop by the external flow, especially when the capillary number is not too small. The collision of two fully deformable drops has also been studied using three-dimensional boundary-integral methods [19, 21-24]. In this case, however, the capillary numbers investigated were relatively large. Furthermore, the thin film drainage and rupture process was not studied systematically since the van der Waals force was not considered in most cases, due to the high computational cost.

Motivated by these proceeding studies and the availability of quantitative and often puzzling experimental data [9, 11, 12], we investigate here the axisymmetric interaction of two equal-sized deformable drops in a bi-axial extensional flow in the creeping flow limit, using the boundary-integral method. An axisymmetric flow was chosen so that relatively fast calculations over broad parameter ranges could be performed to examine the thin film drainage, as well as the overall deformation, with accurate resolution. An adaptive mesh refinement method was used to resolve the local small-scale dynamics within the thin film, while still retaining a reasonable speed of computation.

Computations for collisions in a time-independent flow were carried out to simulate head-on collisions for Ca of $O(10^{-4}-10^{-1})$ and viscosity ratios of $O(0.1-10)$, which is the same range as studied experimentally. Computations were also carried out for collisions in time-dependent flows with the objective of simulating glancing collisions. The results were compared with the experimental results from our earlier studies [9, 11, 12], as well as the scaling theories for thin film drainage [9, 25]. The rationale for

comparing these axisymmetric simulations with the experimental data will be addressed partially in the next paragraph, and partially at the beginning of Section 4.

A primary goal of this numerical study is to investigate the thin film dynamics, which is crucial to understanding the complex and often unexpected experimental results of our earlier studies [9, 11, 12]. An axisymmetric collision allows for a robust and accurate local resolution of the thin gap region where the important physics evolves. However, an obvious question is whether the axisymmetric thin film drainage problem is an adequate approximation of the full three-dimensional (3D) collision process.

The assumptions underlying this approach are two-fold. First is the idea that a fully 3D collision trajectory can be described via the superposition of a relative translational motion along the line of centers, and a rotation of the line of centers. This description is exact if $Ca = 0$ so that the drops are perfectly spherical, and it is approximately true in an asymptotic sense provided $Ca \ll 1$. In this case, one can study the film drainage process for a 3D "glancing collision by studying a head-on collision with the velocity gradient changing as a function of time so that the force along the line of centers is the same as it would be in the glancing collision. The second assumption is that the axisymmetric film for the biaxial flow is an adequate approximation of the film geometry in the 2D straining flow that is obtained in the 4-roll mill. Again, it can be shown that this assumption is asymptotically correct in the limit $Ca \ll 1$. Recently, experiments in our group [12] were carried out to probe the "decomposition" of the collision process, by comparing coalescence times for glancing collisions and for head-on collisions with the shear rate varied with time as described above. The results were experimentally indistinguishable over the full range of capillary number that was covered in the coalescence experiments.

The only way to "exactly" check The only way, potentially, to quantify the approximation inherent using the axisymmetric extensional flow instead of the 2D flow that is used in the experiments would be by comparison of computational results for these two cases. The comparsons that have been carried out show no significant difference for $Ca \ll 1$ [24, 26], though we are doubtful that the existing 3D simulations have enough resolution to maintain accuracy all the way to film rupture.

A secondary objective is to assess the relevance of a classical continuum theory in describing the coalescence process, which occurs with a minimum film thickness of $O(100\,\mathring{\mathrm{A}})$ for the fluids considered here. There are three basic areas of assumption: the fluids are Newtonian with the same properties in the thin film as in the bulk fluid domain; the interface is sharp and characterized by a constant interfacial tension; and the van der Waals force across the film can be approximated as a disjoining pressure based on the local film thickness and a Hamaker constant that is fixed at the value given by Lifshitz theory. In the absence of a molecular theory for the thin film region, the best test that we can make is to compare theoretical predictions of the coalescence process based on the continuum theory with experimentally measured values of the same quantities. The present work represents the first attempt to study the flow-induced coalescence process based upon a continuum model, with predictions at the same parameter values where experiments were carried out in the four-roll mill.

2. NUMERICAL METHOD

The primary objective of this study is to examine the details of the evolution of drop deformation and relative position from the prescribed initial separation up to the event of

the film rupture. A schematic of two deformable drops in a linear axisymmetric flow is shown in Fig. 1. The viscosities of the suspending fluid and the drop fluid are μ_e and μ_d respectively. Both fluids are Newtonian, and the densities are matched. Each drop has an undeformed radius *R*. The undisturbed external flow at infinity is the biaxial extensional flow with the strain rate, G ,

$$\mathbf{u}_\infty = \frac{G}{2}\begin{pmatrix} 1 & 0 & 0 \\ 0 & 1 & 0 \\ 0 & 0 & -2 \end{pmatrix} \cdot \mathbf{x}. \tag{1}$$

2.1. Boundary integral formulation

When the Reynolds number is small, the hydrodynamics of the colliding drops become a Stokes flow problem. Boundary integral methods provide us with a representation of the flow in terms of a distribution of point forces on the interface of the drops [4, 27]. The velocity $\mathbf{u}(\mathbf{x}_0)$ at each interfacial point $\mathbf{x}_0$ can be written, in dimensionless form, in terms of integrals over the surfaces of the two drops $S_1 + S_2$ as

$$\begin{aligned} \mathbf{u}(\mathbf{x}_0) = \frac{2}{1+\lambda}\mathbf{u}^\infty(\mathbf{x}_0) - \frac{1}{4\pi\mu_e(1+\lambda)} \int_{S_1+S_2} \mathbf{G}(\mathbf{x},\mathbf{x}_0)\cdot\mathbf{f}(\mathbf{x})dS(\mathbf{x}) \\ + \frac{1}{4\pi}\frac{1-\lambda}{1+\lambda} \int_{S_1+S_2} \mathbf{u}(\mathbf{x})\cdot\mathbf{T}(\mathbf{x},\mathbf{x}_0)\cdot\mathbf{n}(\mathbf{x})dS(\mathbf{x}). \end{aligned} \tag{2}$$

Here λ is the viscosity ratio (μ_d/μ_e), $\mathbf{x}$ is the spatial variable of integration on the drop surfaces, $\mathbf{f}(\mathbf{x})$ is the jump of the stress across the interface ($[\boldsymbol{\sigma}_e - \boldsymbol{\sigma}_d]\cdot\mathbf{n}$), $\mathbf{n}$ is the unit outward normal vector, and

$$\mathbf{G}(\mathbf{x},\mathbf{x}_0) = \frac{\mathbf{I}}{r} + \frac{\mathbf{rr}}{r^3}, \tag{3}$$

$$\mathbf{T}(\mathbf{x},\mathbf{x}_0) = -6\frac{\mathbf{rrr}}{r^5}. \tag{4}$$

The tensor $\mathbf{G}$ is known as the Stokeslet (free-space Green's function of Stokes flow), $\mathbf{T}$ is the stresslet, $\mathbf{r} = \mathbf{x} - \mathbf{x}_0$, $r = |\mathbf{r}|$, and $\mathbf{I}$ is the unit tensor. The first integral term in Eqn. (2) is referred to as the single-layer potential, whereas the second integral term is known as the double-layer potential. In the present simulations, we assume that the attractive van der Waals force across the thin film can be approximated via a disjoining pressure. Retardation effects for the van der Waals interaction are also considered [18, 28]. Hence, when the interfacial tension is constant (i. e. clean interface), and the drop is neutrally buoyant (i. e. $\rho_e = \rho_d$), $\mathbf{f}(\mathbf{x})$ can therefore be expressed in the form

$$\mathbf{f}(\mathbf{x}) = \left[2\sigma\kappa(\mathbf{x}) - \frac{A_{H,eff}}{6\pi h(\mathbf{x})^3} \right] \mathbf{n}(\mathbf{x}) = f(\mathbf{x})\mathbf{n}(\mathbf{x}), \tag{5}$$

where σ is the interfacial tension, $\kappa(\mathbf{x})$ is the mean curvature of the interface ($2\kappa(\mathbf{x}) = \nabla_s \cdot \mathbf{n}(\mathbf{x})$, where ∇_s is the surface gradient operator), $A_{H,eff}$ is the effective Hamaker constant including retardation effects, and $h(\mathbf{x})$ is the local minimum distance to the other interface.

The above boundary-integral formulation, although formally exact, contains singularities when $\mathbf{x} \to \mathbf{x}_0$. However, methods have been developed to obtain second order numerical approximations. Starting with this standard boundary-integral formulation for the interfacial velocity, the leading order singularity and near-singularity are removed by a suitable subtraction that uses two stokes flow identities [21, 22, 27]. The resulting integrals are then approximated by the trapezoidal rule. It is important to note that this "singularity subtraction" only removes the leading order singularity but

leaves an infinite number of singularities that affect all the higher derivatives of the integrand. Thus, to construct approximations to the boundary integrals with accuracy more than two it is necessary to account for this subtle singular behavior. Here we employ the second order approximation. Also, to facilitate the solution of the integral equation (2). The marginal eigenvalues at $\lambda \to 0$ and $\lambda \to \infty$ are removed by Wielandt's deflation [23, 27, 29]. The result of the leading order singularity and near singularity subtraction and the Wielandt's deflation is the following expression for a modified interfacial velocity

$$\begin{aligned}\mathbf{w}(\mathbf{x}_0)\big|_{S_\alpha} = \frac{2}{1+\lambda}\mathbf{u}^{\infty}(\mathbf{x}_0) - \frac{1}{4\pi\mu_e(1+\lambda)}\int_{S_1+S_2}\mathbf{G}(\mathbf{x},\mathbf{x}_0)\cdot\mathbf{n}(\mathbf{x})\Big[f(\mathbf{x})-f(\mathbf{x}^*)\Big]dS(\mathbf{x}) \\ + \frac{1}{4\pi}\frac{1-\lambda}{1+\lambda}\int_{S_1+S_2}\Big[\mathbf{w}(\mathbf{x})-\mathbf{w}(\mathbf{x}^*)\Big]\cdot\mathbf{T}(\mathbf{x},\mathbf{x}_0)\cdot\mathbf{n}(\mathbf{x})dS(\mathbf{x}) \\ - \frac{1-\lambda}{1+\lambda}\Big[\mathbf{w}(\mathbf{x}_0)+\big\langle\mathbf{w}\cdot\mathbf{n}\big\rangle_{S_\alpha}\mathbf{n}(\mathbf{x}_0)-\big\langle\mathbf{w}\big\rangle_{S_\alpha}\Big].\end{aligned} \tag{6}$$

The interfacial velocity, $\mathbf{u}(\mathbf{x}_0)$, is related to the modified velocity, $\mathbf{w}(\mathbf{x}_0)$, according to

$$\mathbf{u}(\mathbf{x}_0) = \mathbf{w}(\mathbf{x}_0) - \frac{1-\lambda}{2}\big\langle\mathbf{w}\big\rangle \tag{7}$$

Referring back to Eqn. (6), the index α in S_α refers to either surface of drop 1 or 2, $\mathbf{x}_0$ is a fixed point on one of the drop surfaces (S_1 or S_2), $\mathbf{x}^*$ is $\mathbf{x}_0$ for integration on the drop surface containing $\mathbf{x}_0$ (leading order singularity subtraction), and for integration on the other drop surface, $\mathbf{x}^*$ is the point on the surface that is closest to $\mathbf{x}_0$ (near leading order singularity subtraction). The leading order singularity subtraction is made possible by the identities [21, 27],

$$\int_{S_\alpha} \mathbf{G}(\mathbf{x},\mathbf{x}_0)\cdot\mathbf{n}(\mathbf{x})dS(\mathbf{x}) = 0, \text{ and } \int_{S_\alpha} \mathbf{T}(\mathbf{x},\mathbf{x}_0)\cdot\mathbf{n}(\mathbf{x})dS(\mathbf{x}) = \begin{cases} -4\pi\mathbf{I}, & \mathbf{x}_0 \in S_\alpha(\mathbf{x}) \\ 0, & \mathbf{x}_0 \notin S_\alpha(\mathbf{x}) \end{cases}. \quad (8)$$

The quantity $\mathbf{w}(\mathbf{x}_0)$ in the last term of Eqn. (6) comes from the leading order singularity subtraction of the double-layer potential. The quantities $\langle \mathbf{w}\cdot\mathbf{n} \rangle$ and $\langle \mathbf{w} \rangle$, which come from Wielandt's deflation, are area averages for the surface of the drop containing $\mathbf{x}_0$.

We can now non-dimensionalize using the following characteristic scales

$$l_c = R,\ w_c = \sigma/R,\ t_c = \mu_e R/\sigma. \quad (9)$$

The modified interfacial velocity in dimensionless form is then given by

$$\begin{aligned} \mathbf{w}(\mathbf{x}_0)\big|_{S_\alpha} = {} & \frac{2}{1+\lambda} Ca\,\mathbf{u}^\infty(\mathbf{x}_0) - \frac{1}{4\pi(1+\lambda)} \int_{S_1+S_2} \mathbf{G}(\mathbf{x},\mathbf{x}_0)\cdot\mathbf{n}(\mathbf{x})\left[f'(\mathbf{x}) - f'(\mathbf{x}^*) \right] dS(\mathbf{x}) \\ & + \frac{1}{4\pi}\frac{1-\lambda}{1+\lambda} \int_{S_1+S_2} \left[\mathbf{w}(\mathbf{x}) - \mathbf{w}(\mathbf{x}^*) \right]\cdot\mathbf{T}(\mathbf{x},\mathbf{x}_0)\cdot\mathbf{n}(\mathbf{x})dS(\mathbf{x}) \\ & - \frac{1-\lambda}{1+\lambda}\left[\mathbf{w}(\mathbf{x}_0) + \langle \mathbf{w}\cdot\mathbf{n} \rangle_{S_\alpha}\,\mathbf{n}(\mathbf{x}_0) - \langle \mathbf{w} \rangle_{S_\alpha} \right]. \end{aligned} \quad (10)$$

In this equation, Ca is the capillary number ($Ca = \mu_e GR/\sigma$), $\mathbf{u}_\infty$ is the applied bi-axial extensional flow, which can be defined in cylindrical coordinates as

$$\mathbf{u}_\infty = \left(\frac{1}{2} r\,\mathbf{e}_r - z\,\mathbf{e}_z\right), \quad (11)$$

and $f'(\mathbf{x})$ is

$$f'(\mathbf{x}) = 2\kappa(\mathbf{x}) - \frac{A^*_{H,eff}}{h(\mathbf{x})^3}, \quad (12)$$

where $A^*_{H,eff} = A_{H,eff}/6\pi\sigma R^2$ is the dimensionless van der Waals interaction parameter.

2.2. Numerical scheme

2.2.1. Azimuthal integrations

For a given axisymmetric flow, a further simplification can be made by analytical integration around the axis of symmetry using cylindrical coordinates. The resulting formulation takes the form of line integrals. The single-layer and double layer potential terms are then expressed as

$$\begin{aligned}&\int_S \mathbf{G}(\mathbf{x},\mathbf{x}_0)\cdot\mathbf{n}(\mathbf{x})\left[f'(\mathbf{x})-f'(\mathbf{x}^*)\right]dS(\mathbf{x})\\&\quad=\int_C M_{ij}(\mathbf{x},\mathbf{x}_0)n_j(\mathbf{x})\left[f'(\mathbf{x})-f'(\mathbf{x}^*)\right]dl(\mathbf{x})\end{aligned}\tag{13}$$

$$\begin{aligned}&\int_S\left[\mathbf{w}(\mathbf{x})-\mathbf{w}(\mathbf{x}^*)\right]\cdot\mathbf{T}(\mathbf{x},\mathbf{x}_0)\cdot\mathbf{n}(\mathbf{x})dS(\mathbf{x})\\&\quad=\int_C\left[Q_{ijk}(\mathbf{x},\mathbf{x}_0)n_k(\mathbf{x})w_j(\mathbf{x})-Q'_{ijk}(\mathbf{x},\mathbf{x}_0)n_k(\mathbf{x})w_j(\mathbf{x}^*)\right]dl(\mathbf{x})\end{aligned}\tag{14}$$

where the line integral contour, C, is taken over the circumferential surfaces of the drops in the ϕ=0 half-plane.

The components of M_{ij} and Q_{ijk} are available in Pozrikidis [27], and the components of Q'_{ijk} are given in Davis [26]. The components involve the complete elliptic integrals of the first and second kind. These elliptic integrals are calculated using the polynomial approximations of Abramowitz and Stegun [30] and the asymptotic expansions of Lee and Leal [31], as indicated in Davis [26]. The numerical integrations of Eqn. (13) and (14) are carried out using the trapezoidal rule, along the discretized trace C of the drops.

2.2.2. Discretization: Adaptivity through dynamic parametrizations and mesh refinements

We employ an adaptive spatial discretization to achieve accurate resolution of the widely different length scales of the coalescence problem while attempting to minimize

the computational cost. The adaptivity is obtained by dynamically changing the parametrization of the interface (which controls the distribution of computational points on the interface) as in [32-34] and by mesh refinement. The curve C is represented at all times in parametric form by $\mathbf{x}(\beta,t) = (r(\beta,t), z(\beta,t))$, where $0 \le \beta \le 1$ and all the variables in physical space are expressed in terms of β. The parameter β is discretized uniformly into $n+1$ points. The spacing of these marker points on the interface is controlled by the infinitesimal arclength metric is given by

$$s_\beta(\beta,t) = \frac{\partial s}{\partial \beta} = \sqrt{r_\beta{}^2 + z_\beta{}^2}\ . \tag{15}$$

We can select the parameterization [32-34] so that

$$s_\beta(\beta,t) = P(\beta)\, L(t)\,, \tag{16}$$

where $P(\beta) > 0$ and satisfies the constraint

$$\int_0^1 P(\beta) d\beta = 1\,. \tag{17}$$

In Eqn. (16), $L(t)$ is the total length of the curve C at time t, i.e.

$$L(t) = \int_0^1 \frac{\partial s}{\partial \beta'} d\beta' = \int_0^1 P(\beta') L(t) d\beta' = L(t) \int_0^1 P(\beta') d\beta'\,. \tag{18}$$

Note that if $P(\beta) \equiv 1$ then all the interface markers (nodes) will be equally distributed in arclength. Instead of this choice, we select $P(\beta)$ based on the geometry of the drop surfaces to obtain the required non-uniform node distribution. Specifically, when the deformation of the interfaces in the gap region is not large (i.e. the interfaces are not dimpled) $P(\beta)$ is set to be similar to a step function. It has small constant value ($P_{\min}$) near the defined gap region and a large constant value ($P_{\max}$) away from the gap. This

function was constructed analytically by connecting smoothly the specified $P_{\min}$ and $P_{\max}$ using a third order polynomial [35]:

$$P(\beta) = \begin{cases} P_{\min} & 0 \le \beta \le \delta \\ P_{\min} + (P_{\max} - P_{\min}) Q(\dfrac{\beta - \delta}{\varepsilon}) & \delta \le \beta \le \delta + \varepsilon \\ P_{\max} & \delta + \varepsilon \le \beta \le 1 \end{cases}, \tag{19}$$

where δ is the width of the region across which $P = P_{\min}$, and ε is the width of the transition region across which $P(\beta)$ changes according to

$$Q(\xi) = 35\xi^4 - 84\xi^5 + 70\xi^6 - 20\xi^7 . \tag{20}$$

The polynomial $Q(\xi)$ is such that: $Q(0) = 0$ and $Q(1) = 1$, and its three derivatives vanish at $\xi = 0$ and 1. Note that not all of the parameters in Eqn. (19) are independent. Using the constraint (17) it follows that

$$P_{\max} = \frac{1 - P_{\min}(\delta + 0.5\varepsilon)}{1 - (\delta + 0.5\varepsilon)} . \tag{21}$$

Now, the spacing between two consecutive nodes i and $i+1$ in the region where $P(\beta)$ assumes the constant value $P_{\min}$, i.e. the minimum node spacing $\Delta s_{\min}$ satisfies:

$$\Delta s_{\min} = L(t) \int_{\beta_i}^{\beta_{i+1}} P(\beta') d\beta' = L(t) P_{\min} \frac{1}{n} . \tag{22}$$

We select $\Delta s_{\min}$ to be 70% of the minimum film thickness $h_{\min}$ and hence

$$P_{\min} = 0.7 h_{\min} \frac{n}{L(t)} . \tag{23}$$

The parameter δ can be defined by matching the region across which $P = P_{\min}$ to the end of the pre-defined thin gap (s_{gap}):

$$\Delta s_{gap} = L(t) \int_0^{\delta} P(\beta') d\beta' = L(t) P_{\min} \delta \;\Rightarrow\; \delta = s_{gap} \big/ L(t) P_{\min} . \tag{24}$$

To define the thin gap region ($0 \le s \le s_{gap}$), s_{gap} is chosen by either the position where the meridian curvature (κ_m) is maximum or where the radial extent is $O(Ca^{1/2})$. The parameter ε was set to 0.3.

In order to maintain an adequate resolution globally we set the maximum allowed node spacing (outside the node region) $\Delta s_{\max}$ to be 0.01-0.02. This was achieved by controlling the number of nodes n. Because

$$\Delta s_{\max} = L(t) P_{\max} \frac{1}{n}, \tag{25}$$

we can use the constraint (17) to determine the required n.

When the interface is dimpled, to adjust to the geometry of the interface, we employ different $P(\beta)$ that connects smoothly four values, P_{center}, $P_{\min}$, P_{gap}, and $P_{\max}$. Here P_{center} and P_{gap} correspond to the values of P at the center and at the end of the gap, respectively. More specifically, in this case $P(\beta)$ is defined as

$$P(\beta) = \begin{cases} P_{center} + (P_{\min} - P_{center}) Q(\dfrac{\beta}{\delta_{\min}}) & 0 \le \beta \le \delta_{\min}, \\ P_{\min} + (P_{gap} - P_{\min}) Q(\dfrac{\beta - \delta_{\min}}{\delta_{gap}}) & \delta_{\min} \le \beta \le \delta_{\min} + \delta_{gap}, \\ P_{gap} + (P_{\max} - P_{gap}) Q(\dfrac{\beta - (\delta_{\min} + \delta_{gap})}{\varepsilon}) & \delta_{\min} + \delta_{gap} \le \beta \le \delta_{\min} + \delta_{gap} + \varepsilon, \\ P_{\max} & \delta_{\min} + \delta_{gap} + \varepsilon \le \beta \le 1, \end{cases} \tag{26}$$

and we set

$$P_{center} = 0.7 h_{center} \frac{n}{L(t)}, \tag{27}$$

$$P_{\min} = 0.7 h_{\min} \frac{n}{L(t)}, \tag{28}$$

$$P_{gap} = 0.7 h_{gap} \frac{n}{L(t)}, \tag{29}$$

where h_{center} and h_{gap} are the thickness of the film at the center of the gap and at the end of it, respectively. Again, ε is fixed to 0.3, $\Delta s_{\max}$ is set to 0.01-0.02, and required n is determined from the constraint (17). Figure 2 shows typical examples of $P(\beta)$ profiles for two cases of (19) and (26).

Initially, the simulation is run with uniform node spacing (n = 200 on one-half of a drop) until the drops are in close proximity. Then, the non-uniform node spacing is introduced. Usually mesh refinement in β was conducted 3 – 8 times during a simulation, based on the film thickness. The interpolation of the shape was carried out spectrally using the fast-Fourier transform (FFT) [36]. Figure 3 shows a typical example of the evolution of the interface shape in the gap region as well as the non-uniform node distribution constructed using the methods described above. The nodes are plotted every 4 points in the figure.

The first procedure of the calculation is to compute all geometric interfacial quantities from the known position of the interface. Next, the velocity components are calculated by solving Eqn. (10) iteratively. To accelerate the convergence we employ extrapolated values from previous time steps as initial estimates. A simple first order extrapolation was used for each velocity component [26, 36]. The interface position is then updated by the kinematic condition,

$$\frac{\partial \mathbf{x}}{\partial t} = \mathbf{u} + u_A \mathbf{t}, \tag{30}$$

where $\mathbf{u}$ is the interfacial velocity obtained via the boundary-integral calculation, and $u_A\mathbf{t}$ is an auxiliary tangential velocity, used to maintain the desired distribution of nodes at the interface while the interface shape remains unaltered [21-23]. This auxiliary velocity [36] is calculated at each node (j) using

$$u_{A,j} = -\mathbf{u}_j \cdot \mathbf{t}_j + \int_0^{\beta_j} \left\{ \frac{\partial s}{\partial \beta'} \kappa_m \mathbf{u} \cdot \mathbf{n} - P(\beta') \left\langle \frac{\partial s}{\partial \beta} \kappa_m \mathbf{u} \cdot \mathbf{n} \right\rangle \right\} d\beta' , \tag{31}$$

where

$$\left\langle \frac{\partial s}{\partial \beta} \kappa_m \mathbf{u} \cdot \mathbf{n} \right\rangle = \int_0^1 \frac{\partial s}{\partial \beta} \kappa_m \mathbf{u} \cdot \mathbf{n} \, d\beta . \tag{32}$$

A second-order Rugge-Kutta method is used to integrate the kinematic condition, Eqn. (30). The stability criterion for time integration [37] is

$$\Delta t \le \Delta s_{\min} , \tag{33}$$

where the dimensionless time, t , is defined earlier as $t' / \left(\mu_e R / \sigma \right)$, and $\Delta s_{\min}$ is the minimum separation between the nodes. This criterion can be expressed as

$$\Delta (t' G) \le Ca \, \Delta s_{\min} . \tag{34}$$

The meridian curvature (κ_m), azimuthal curvature (κ_ϕ), and components of the normal vector (n_r and n_z) are

$$\kappa_m = (r_\beta z_{\beta\beta} - z_\beta r_{\beta\beta}) / s_\beta^{\,3} , \tag{35}$$

$$\kappa_\phi = n_r / r , \tag{36}$$

$$n_r = z_\beta / s_\beta , \text{ and } \; n_z = -r_\beta / s_\beta , \tag{37}$$

where the subscript β stands for differentiation with respect to that variable [32-34]. The mean curvature is one-half the sum of the meridian and azimuthal curvatures:

$$\kappa = \frac{1}{2}(\kappa_m + \kappa_\phi). \tag{38}$$

For the end points on the axis of symmetry, $\kappa = \kappa_m$. It is crucial to resolve accurately above mentioned geometric quantities. For this reason, we adopted spectral methods. The first and second derivatives of the coordinates with respect to β were calculated pseudo-spectrally using FFT for calculating the geometric properties. The details of the spectral methods are available in Baldessari [36].

2.2.3. Convergence tests

The convergence of the boundary-integral method was tested by varying the node spacing. The Hamaker constant, A_H, is assigned the value 3.199×10^{-21} J, which makes it possible to directly compare this study with our earlier experimental studies [9, 11, 12]. The Lifshitz theory is used to estimate the Hamaker constant, using the refractive index of polybutadiene (PBd, n_{PBd} =1.515) and polydimethylsiloxane (PDMS, n_{PDMS} =1.403) and the main electronic absorption frequency ($\nu_e = 3\times10^{15} s^{-1}$) [18, 28, 38]. The estimated Hamaker constant is a typical value for a polymer/polymer system [38]. Three different viscosity ratios of 0.19, 1.2, and 6.8 were studied, and a range of drop radius from 1 – 70 μm. For a fixed capillary number, the drop size only affects the dimensionless Hamaker constant ($A^* = A_H / 6\pi\sigma R^2$), as shown earlier in the governing equation of the boundary-integral method (cf. Eqn. (10)). The drops are initially positioned with a center-to-center distance of $4R$. The experimentally measured interfacial tensions are used [11] (σ = 4.6, 4.8, and 5.0 mN/m for λ = 0.19, 1.2, and 6.8 respectively).

Figure 4 shows the evolution of the thin film for $Ca = 0.015$, $\lambda = 0.19$, and $A^* = 4.99\times10^{-11}$ ($R = 27.2$ μm and $\sigma = 4.6$mN/m). The minimum film thickness, $h_{\min}$, the film thickness at the center of the film, h_{center}, and the radius of the thin film (or dimple), a, as a function of time are plotted in the figure. The data shown in the figure are the results of three different types of calculation: one pair of solutions using a *uniform* node spacing (n = 500 and 1000); a second set of three solutions using the step-function shaped node distributions having three different Δs in the thin film region (referred as the step 1 for $\Delta s = 0.002$, step 2 for $\Delta s = 0.001$, and step 3 for $\Delta s = 0.0005$), and a single interpolation at $h_{\min} \cong 0.03$; and a pair of solutions using the adaptive method (adaptive 1 for re-meshing 7 times up to Δs =0.0005 and adaptive 2 for re-meshing 8 times up to Δs =0.0003).

As shown in Figure 4, a Δs of 0.0005 was necessary to retain enough accuracy in the region where the interface ruptures. This value of Δs approximately corresponds to the critical film thickness for coalescence. The computation speed of the boundary-integral method is proportional to $O(n^2)$. Therefore, the typical small critical film thickness (or small dimensionless Hamaker constant) combined with the small capillary number is a restrictive condition for numerical studies of the coalescence process. On the other hand, when the van der Waals force was not included, a Δs of 0.002 was enough to obtain the converged result up to the film thickness of $O(10^{-4})$. We view the solution with Δs =0.0005 and a single interpolation at $h_{\min} \cong 0.03$ (i.e. the calculation labeled "step 3") as the most accurate, but it took a very long time to compute since the very small mesh size is carried over more than two decades of film width from 0.03 to $O(10^{-4})$.

The convergence test results are summarized in Table 1, including the coalescence time, tG_{coal}, and the error of tG_{coal} relative to the t_dG_{coal} of step 3. The volumes of drops for the axisymmetric simulations remained constant to 0.04 % for the adaptive methods. The adaptive method speeds up the calculation by more than 10 times compared to step 3, while still maintaining accuracy.

3. RESULTS FOR HEAD-ON COLLISIONS

In this section we present numerical results for collisions with a time-independent flow, which simulate the "head-on collision" experiments. The results provide the details of the flow-induced collision process, including the thin film dynamics, which was impossible to observe in the four-roll mill experiments. We first discuss and illustrate qualitatively the evolution of the overall drop shape and the thin-film shape for the case of $\lambda = 0.19$. Then, we compare experimental data with predictions of drainage time as a function of capillary number and viscosity ratio for a fixed drop size of $R = 27.2$ μm, discussing the general behavior of the collision process. The effect of drop size and the critical film thickness for coalescence are also discussed for all three experimental viscosity ratios.

3.1. Drop shape evolution

The evolution of the drop shape, from the prescribed initial separation up to the event of coalescence, was calculated. The results were also compared with the experimental data of our earlier studies [9, 11]. To briefly summarize the experimental studies, we measured the drainage time, t_dG, which is the period from the point when the center-to-center distance is one drop diameter ($d = 2R$) to the instant of coalescence. However, we

could not experimentally study the dynamics of the thin film formed by the colliding drops.

Figure 5 shows a comparison between an experimentally measured collision trajectory and a calculated trajectory. The center-to-center distance (d/R) as a function of dimensionless time (tG) is plotted for Ca = 0.0207, λ = 0.19, and A^* = 4.99×10^{-11} (R = 27.2 μm and σ = 4.6mN/m). This capillary number is one of the largest values that we considered in our previous experiments. The insets show the calculated overall drop shape at $d = 2R$ and the steady drop shape at tG = 2.041. The experimental data and the numerical calculation show excellent agreement for the drainage time as well as the deformation of the drops.

The dynamics of the thin film between colliding drops plays an important role in coalescence, since the film must drain to a critical film thickness (or at least achieve an unstable shape) for the film to rupture. The interface of the drops may either remain spherical, flattened, or dimpled near the area of apparent contact during the film drainage process, depending on the magnitude of the hydrodynamic force relative to the magnitude of capillary forces due to the interfacial tension. Therefore, the flow-induced coalescence of drops is strongly governed by the capillary number.

Figure 6(a) shows the evolution of the local minimum film thickness, $h_{\min}$, the film thickness at the center of the film, h_{center}, and the radial extent of the film, a, for Ca = 0.015, λ = 0.19, and A^* = 4.99×10^{-11}. The same type of data without the van der Waals force ($A_H = 0$) are also presented by dotted lines. Figure 6(b) shows the evolution of the thin film shape at the points indicated in Fig. 6(a) by the open circles. As time progresses, the film thickness decreases, the shape of the film becomes flattened, and eventually a

dimple is formed. After the dimple is fully formed, the rate of the film drainage is significantly slowed, as shown in Fig. 6(a). At this stage, the thin film pressure reaches the maximum value of the capillary pressure ($O(2\sigma/R)$). The pressure becomes relatively uniform over the majority of the gap region, with the pressure gradient only occurring near the rim of the dimpled region [18]. As the film thins, the strength of the van der Waals force increases. Finally, the evolution of the film shape (mostly $h_{\min}$) starts to deviate from the case without the van der Waals force, and eventually the film ruptures at the rim of the dimple. The drainage time, $t_d G$, is indicated in Fig. 6(a).

The mean curvatures for the entire drop are plotted in Fig. 7, at the moments indicated earlier in Fig. 6. The variations in curvature occur over the front half of the drop near the gap region, and the deformation of the back of the drop remains almost constant. After the dimple is fully formed (beyond the 4th plot), the interface is almost flat ($\kappa \cong 0$) near the center of the film, and the deformation increases only near the rim of the dimple.

On the other hand, when the capillary number is relatively small, the thin film dynamics are quite different from the case of the higher capillary number. Figure 8 shows the same types of data for Ca = 0.0008, λ = 0.19, and A^* = 4.99×10^{-11}. In Fig 8(a), presented by dotted lines are the data without the van der Waals force ($A_H = 0$). First, the initial film thickness (i. e. the thickness when the center-to-center distance is $2R$) is much smaller than the case of the higher capillary number (the 3rd point in Fig. 8(a)). The thin film remains almost spherical almost all through the film drainage, due to the smaller capillary number. The drainage time is much shorter than in the higher capillary number case, where the film drainage process dominantly occurs with the dimpled configuration.

The mean curvatures for the entire drop are plotted in Fig. 9, at the moments indicated in Fig. 8. The back of the drop remains almost spherical ($2\kappa \cong 1$), and the variations in curvature occur only near the gap region. Both the front and back half of the drop are almost spherical for the first plot ($h_{\min} \cong 0.2$). As the film thins, the deformation near the small gap region increases (the interfaces are flattened), and the interface eventually becomes dimpled right before the film rupture. The inset in the figure shows the mean curvature of the drop at $d = 2R$ (3^{rd} plot in the main figure).

3.2. Drainage time for R = 27.2 μm

In this section, we will present the predicted and experimentally measured drainage time data for a fixed drop size of R = 27.2 μm at various viscosity ratios and discuss the general behavior of the collision process. The drainage time as a function of Ca for R = 27.2 μm at viscosity ratios of 0.19, 1.2, and 6.8, is shown in Fig. 10. The results of the simulations and experiments are shown by the solid symbols and open symbols respectively. The drainage times are scaled by the radius of the drop raised to the 5/4 power in order to allow for direct comparison with the experiments, where this scaling was found empirically to reduce the drainage times for different size drops to a single curve [9, 11]. The experimental data, in fact, contain sets of data for different drop sizes including R = 27.2 μm. Also shown in Fig. 10 are straight lines with various slopes, which we explain below.

It was suggested in our previous studies that the experimental data increased with Ca as $Ca^{3/2}$. This appeared to be consistent with predictions from a very simple scaling theory, which assumes that thin film is a flat disk, and leads to the prediction [9, 25],

$$t_d G \sim \sqrt{f(\lambda)}\,\lambda\, Ca^{3/2}\left(\frac{1}{h_c}\right), \tag{39}$$

where h_c is the dimensionless critical film thickness (h_c'/R) for film rupture, and $f(\lambda)$ is a known function that depends only weakly on λ as $f(\lambda) \sim \lambda^{0.1}$. [9]. As long as the critical film thickness is independent of Ca the previously proposed scaling is valid. From a scaling standpoint, the critical film thickness will be reached when the magnitude of the van der Waals force (i.e. the disjoining pressure) becomes comparable to the capillary force (i.e. the capillary pressure) at least locally. The disjoining pressure is approximately A_H / h'^3, where A_H is the Hamaker constant, and h' is the dimensional film thickness. When the drop is dimpled, the minimum film thickness will occur near the rim of the thin film. The magnitude of the stabilizing capillary pressure, on the other hand is σ / ℓ_c, where σ is the interfacial tension and ℓ_c is the local radius of curvature. The ratio of these two pressures is

$$\tilde{A} \equiv \frac{A_H / h'^3}{\sigma / \ell_c}. \tag{40}$$

If $\ell_c = R$, $\tilde{A}$ is just 6π times the dimensionless Hamaker constant A^* that appeared previously in Eqn. (12). The onset of film rupture is expected when $\tilde{A} = O(1)$, and then

$$h_c = \left(\frac{h'}{R}\right)_c \sim \left(\frac{A_H}{\sigma R^2}\right)^{1/3}\left(\frac{\ell_c}{R}\right)^{1/3} = \left(A^*\right)^{1/3}\left(\frac{\ell_c}{R}\right)^{1/3}. \tag{41}$$

The scaling theory of Chesters [25] assumed $\ell_c = R$ so that h_c is independent of Ca. However, it is clear from results like Fig. 6 that ℓ_c at the rim of the film is much smaller than *R*. We have not been able to establish a rigorous asymptotic argument for the

appropriate scaling. A most conservative guess is that ℓ_c has the same scaling as the radius of the dimple, $\ell_c \sim RCa^{1/2}$. Quite possibly, the power on Ca should be larger than 1/2. In any case, if we adopt this assumption, we see

$$h_c = \left(\frac{h'}{R}\right)_c \sim \left(A^*\right)^{1/3} Ca^{1/6} \tag{42}$$

It then follows from (33) that

$$t_d G \sim \sqrt{f(\lambda)}\lambda Ca^{4/3} A^{*-1/3}. \tag{43}$$

This suggests that the dimensionless drainage time should scale as $Ca^{4/3}$ rather than $Ca^{3/2}$.

A line with a slope of 4/3 is also shown in Fig. 10. It is difficult to determine whether the data matches $Ca^{4/3}$ (dashed line) better than $Ca^{3/2}$ (solid line). In fact the slope changes with Ca (we will discuss the data for the smallest values of Ca shortly), and there is also reason to believe that the slope will change again at larger Ca once the internal circulation driven by the external flow becomes strong enough to affect the film drainage process [20]. We will return to question of whether h_c is independent of Ca or dependent on Ca as suggested by Eqn. (42) shortly.

First, however, we note the distinct change in the dependence of drainage time on Ca that occurs for the lowest values of Ca. In this regime, drops near the contact point remain almost spherical during the film drainage, as shown earlier. The transition occurs when the film drainage in the dimpled configuration is no longer a significant fraction of the total drainage time. In this case, the influence on the drainage process of the weak

($O(Ca)$) overall deformation of the drops due to the external flow increases [18]. The drainage time from the simulation data scales as $t_d G \sim Ca$.

On the other hand, a simple scaling theory for a non-dimpled drop predicts [9]

$$t_d G \sim \frac{1}{f(\lambda)} \lambda \left(h_0\right)^{1/2}, \tag{44}$$

where h_0 is the dimensionless initial film thickness (h_0' / R) at $d = 2R$, assuming that $h_0 \gg h_c$. If each drop deformed as though it were an isolated drop, the initial film thickness should scale with the capillary number as $h_0 \sim Ca$ according to the small deformation theory of Taylor [2]. Thus the drainage time would expected to scale as $t_d G \sim Ca^{1/2}$. Due to hydrodynamic interactions between the drops, h_0 calculated by the boundary-integral simulation actually shows a weaker dependence, $h_0 \sim Ca^{0.8}$, for the entire range of capillary numbers, as shown in Fig. 11.

The experimental data also show a transition in behavior at the lower values of the capillary number. The simulation result correctly predicts the capillary number at which the transition occurs. However, the dependence of the experimental data is not Ca or $Ca^{1/2}$. The experimental drainage time becomes nearly independent of the capillary number. Especially when $\lambda = 0.19$, the drainage time appears to reach a plateau for the lower capillary numbers. One thing to note is that since the drops remain almost spherical at the lower capillary numbers, the experimental error in the determination of the initial point, when $d = 2R$, may have a significant effect on measured value of the relatively short drainage time. It is possible that experimental error may be at least part of the

reason for the difference in the experimental and theoretical results for the lowest capillary number range.

The dimensionless lateral extent of the dimpled region, a, as a function of capillary number is shown in Fig. 12. Over most of the range of Ca, the film radius scales with Ca as $Ca^{1/2}$, which is consistent with the prediction of the scaling theory using a quasi-steady force balance,

$$a \sim \sqrt{f(\lambda)}\, Ca^{1/2}. \tag{45}$$

In these cases, a attains a steady state value (cf. Fig. 6) and it is this value that is plotted in Fig. 12. There is a deviation from $a \sim Ca^{1/2}$ for the lower capillary numbers since the film ruptures at the center of the drops, and this happens before the dimple is fully formed, as shown earlier in Fig. 8. In this case, a is time-dependent and we report the largest value attained, which appears just before rupture.

The numerical results for all three viscosity ratios are shown in Fig. 12. As the viscosity ratio increases, the transition from "dimpled" to "not dimpled" shapes occurs at smaller values of the capillary number. The thickness of the thin film just prior to the onset of dimpling (where it is nearly flat) is shown in Fig.13, for all three viscosity ratios, as a function of Ca. After the dimple is fully formed, the rate of the film drainage significantly slows down. Therefore, the regime of capillary number where the majority of the film drainage process occurs with a dimpled configuration, starts at a lower capillary number as the viscosity ratio increases.

The scaling theory [9] is predicated on the assumption that a dimple will form when the pressure in the thin film becomes the same order as the capillary pressure ($2\sigma/R$). This suggests

$$h_{dimple} \sim f(\lambda) Ca\,. \tag{46}$$

The numerical results in Fig. 13, however, show that the onset of dimpling occurs at a film thickness that scales as $Ca^{1.1}$ for $\lambda = 6.8$, $Ca^{0.95}$ for $\lambda = 1.2$, and $Ca^{0.83}$ for $\lambda = 0.19$. We cannot explain the weaker dependence of h_{dimple} on Ca for the lower viscosity ratio systems.

As we already saw in Fig. 10, the simulation slightly overestimates the drainage time for the higher viscosity ratios for a drop of radius $R = 27.2\mu$m. The drainage time as a function of viscosity ratio for $R = 27.2$ μm and $Ca = 0.004$ is shown in Fig 14. The solid and open symbols are the simulations and experiments respectively. The simulation results predict that the drainage time scales as $t_d G \sim \lambda$. This result is also consistent with the scaling theory, as shown in Eqn. (39), but is significantly different from the experimental observations, where $t_d G \sim \lambda^{0.8}$. The molecular weight of polybutadiene (drops) was changed to increase the viscosity ratio in the experiment. Hence, one might suppose that this is a source of the difference. There is a measurable change in the interfacial tension as noted earlier, but this is already accounted for in the comparisons shown in Fig 10. However, the van der Waals interaction does not change due to a change in the molecular weight, and the molecular weights used here are below the threshold where measurable slip occurs at the interface [39]. Hence, at this point, we simply do not know how to explain the discrepancy in the viscosity ratio dependence of the drainage time.

3.3. Drainage time as a function of the drop radius, *R*

We next examine the effects of the drop size on the drainage time. For a fixed capillary number, a change in the drop radius only affects the dimensionless Hamaker constant ($A^* = A_H / 6\pi\sigma R^2$) as mentioned earlier. In particular, decrease of the drop radius results in an increase of the dimensionless Hamaker constant.

Figure 15 shows the drainage time as a function of Ca for various values of A^* at $\lambda = 0.19$. The radius of the drop ($R = 1 - 70$ μm) and the corresponding dimensionless Hamaker constant ($A^* = 3.69\times10^{-8} - 7.53\times10^{-12}$) are indicated in the figure. Also shown are the experimental data for $R = 27.2$, 40.1, and 45.4 μm. In this case, the drainage times are not scaled by the radius of the drop. The predicted drainage time increases with a decrease of A^* (or an increase of R). This is in qualitatively accord with expectations from Eqn. (43), though we shall see shortly that the scaling is slightly different. For the larger drop size (or smaller values of A^*) there is a clear transition in slope from Ca^m ($m > 1$) to Ca at an intermediate value of Ca. However, for the smallest drops (i. e. the largest A^*), the drainage time is proportional to Ca for almost the full range of Ca values. This is because the dimensionless critical film thickness is increased with increase of A^* (in qualitatively accord with Eqn. (42)), and hence coalescence occurs via the nose rupture mode, before a dimple can form.

For the smallest drops, $R = 1$ μm, the dimple-shaped film drainage is only dominant (i. e. takes up over 70% of the drainage time), if $Ca \geq 0.05$. On the other hand, for the largest drops, $R = 70$ μm, the dimple-shaped film drainage becomes dominant (over 70% of $t_d G$) when $Ca \geq 0.004$. At the same time, the scaling $Ca^{4/3}$ for the dimpled configuration is valid only as long as the drainage process is not affected significantly by

the internal circulation within the drops that is driven by the external flow. Indeed, Nemer *et al*. [20] have shown that there is a value of Ca beyond which drainage can be completely inhibited by the coupling to this flow. If this occurs when $h > h_c$, coalescence is impossible.

Therefore, for R = 1 μm, there is only a small range of the capillary numbers ($O(0.05) \le Ca \le O(0.1)$) where $t_d G \sim Ca^{4/3}$, before the internal circulation due to the ambient flow affects coalescence. In contrast, a relatively wider range of capillary numbers ($O(0.004) \le Ca \le O(0.015)$) exists for R = 70 μm. In this region, the drainage time scales with the capillary number as $t_d G \sim Ca^m$, and the exponent m appears to be a weakly increasing function of the drop size. $m = 1.26$ for R = 1 μm; $m = 1.26$ for R = 3 μm; $m = 1.28$ for R = 10 μm; $m = 1.34$ for R = 27.2 μm; $m = 1.38$ for R = 70 μm. The experimental data also show this slight change in the dependence on Ca with change in R. It will be noted that these values for m are quite near the value 4/3 suggested by the scaling theory, especially for the larger drops. The small drops may be affected by internal circulation before reaching the full 4/3 value.

The experimental drainage times and the calculated drainage times are precisely matched only for R = 27.2 μm. The experimental drainage times for R = 45.4 μm are even longer than those of the simulation for R = 70 μm. The experimental data show a much stronger dependence on the drop size than the simulation. As mentioned in the previous section, the experimental data for the lower capillary numbers do not show any agreement with the calculated values for any size of the drops.

Figures 16 and 17 show the same type of data for various drop sizes at $\lambda = 1.2$ and 6.8 respectively. The results qualitatively show the same behavior as described above for $\lambda = 0.19$. At the lower capillary numbers, the drainage time scales as $t_d G \sim Ca$ independently of the drop size. At the higher capillary numbers, for $\lambda = 1.2$, the slopes of $t_d G$ versus Ca are 1.30, 1.34, 1.36, 1.36, and 1.42, with the increasing drop size indicated in the figure. For $\lambda = 6.8$, the slopes are 1.32, 1.36, 1.35, and 1.38, with the increasing drop size. The drainage time scales with the slightly higher exponent of Ca than $\lambda = 0.19$.

3.4. The critical film thickness

The critical film thickness for coalescence is an important length scale from a scaling point of view. For present purpose, we view the critical film thickness as representing the length scale at which the van der Waals forces become important, but there is clearly some arbitrariness in extracting this length scale from the computational results. In the present work, we do this by comparing the time evolution of the film thickness with and without the van der Waals forces. Specifically, as shown in Fig. 6(a), the critical film thickness is defined by the crossing point of the vertical line at $\left(t_d G\right)_{coal}$ with the curve representing the time evolution of the minimum film thickness without the van der Waals force [16, 25]. Three different sets of results are shown in the following figures representing the dependence of h_c on λ, Ca, and A^*.

First in Fig. 18, we plot h_c versus λ for four different drop sizes (i. e. four different values of A^*), all measured at $Ca = 0.008$ where we expect the scaling theory outlined in

Eqn. (39) - (43) to be valid for all four values of R. It is suggested in Eqn. (42) that h_c increases very weakly with λ. Since $f(\lambda) \approx \lambda^{0.1}$, it follows that $h_c \sim \lambda^{0.017}$. We see from Fig. 18, however, that there is a slight, but consistent increase as $h_c \sim \lambda^{0.07}$. If we refer to Eqn. (39), this would imply that $t_d G \sim \lambda^{0.98}$ instead of the result expected from the scaling relations Eqn. (42), $t_d G \sim \lambda^{1.033}$. Clearly, these are indistinguishable (cf. Fig. 14), but both differ from the experimental result $\lambda^{0.8}$.

Next, in Fig. 19, we plot h_c as a function of Ca for $\lambda = 0.19$ and several different drop sizes ranging in radius from 1 – 70 μm. We are specifically interested in the scaling behavior for the range of capillary number which is large enough that the film drainage dominantly occurs in the dimpled film configuration, but small enough that the influence of the internal circulation (driven by the exterior flow) on the film drainage rate is negligible. Based on our previous discussions, it is clear that the relevant range of Ca depends on the drop size, corresponding to larger Ca for smaller drops and smaller Ca for the larger drops. The scaling prediction from Eqn. (42) is that h_c should vary as $Ca^{1/6}$. We show a straight line with slope 1/6 in the figure. If we fit data in the range of Ca where the curves define a straight line we find $h_c \sim Ca^{0.15}$. Although this would seem to provide strong evidence that the scaling assumptions in deriving Eqn. (42) are correct, it is clear that some variation in the number 0.15 would be seen depending on which precise points we choose to include in the curve fit.

Finally, we plot h_c versus A^* for the three values of λ and a fixed $Ca = 0.008$ in Fig. 20. The scaling prediction from Eqn. (42) is that this should scale as $A^{*1/3}$ but the

measured slope from the numerical predictions is slightly different, namely $\left(A^*\right)^{0.3}$. In effect, this predicts that the drainage time should scale as $t_d G \sim R^{0.6}$ for fixed Ca. On the other hand, the experimental data (taken for drops in the size range from 27 – 50 μm) was found empirically to scale as $R^{5/4}$. This is a major discrepancy between the experimental results and the computational predictions. We do not understand the source of this difference. We are currently carrying out new experiments to vary the drop size over a wider range, and to introduce "molecular" calculations in the thin films when the film thickness reaches a few hundred angstroms.

3.5. Critical conditions for head-on collision

Since the time available for film drainage is not limited in a head-on collision, one might expect that coalescence will occur regardless of Ca. However, both numerical simulations and asymptotic analyses of the flow-induced coalescence of drops show that the internal circulation within the drop, caused by the outer flow, can influence the drainage of the thin film and arrest the film drainage at high Ca [19, 20], hence leading to a critical capillary number even for a head-on collision. We were not able to observe these phenomena in our earlier experimental studies [9, 11]. Drops remain in contact for a long time but eventually tilt from the shear plane (i. e. x-y plane in planar extensional flow generated by the four-roll mill) at high Ca.

A numerical example of arrested coalescence in a head-on collision is shown in Fig. 21, which illustrates the existence of a critical Ca. Figure 21 shows the film evolution for two different capillary numbers at $A^* = 3.93\times10^{-9}$ and $\lambda = 1.2$. The drops coalesce for $Ca = 0.05$ (dashed line), but the thin film reaches a stationary configuration due to

inhibition of the drainage process via coupling with the internal circulation for Ca = 0.055 (solid line). The insets in the figure show the stationary drop shape and the film profile at tG = 100.

Nemer *et al*. [20] predicted the critical conditions for coalescence based on an asymptotic analysis of the thin film, which includes the effect of the internal circulating flow. The viscous force along the line of centers, F , due to the undisturbed external flow for two touching spherical drops, can be expressed in the form [40, 41]

$$F = 2 f(\lambda) \mu_e G R^2 , \tag{47}$$

where $f(\lambda)$ is 11.306, 14.022, and 17.143 for λ = 0.19, 1.2, and 6.8 respectively [41]. By combining Eqn. (47) with the Eqns.(16) and (18) from reference [20], the critical capillary number for the head-on collision can be written in the form,

$$Ca_c = 0.7866 \pi^{5/9} f(\lambda)^{-1/3} \lambda^{-2/3} A^{*\,1/9} . \tag{48}$$

The critical capillary number obtained numerically is plotted in Fig. 22 as a function of the dimensionless Hamaker constant, together with the asymptotic formula (48). The results show good agreement with the prediction of the asymptotic analysis of Nemer *et al*. [20]. The critical capillary number is a weak function of the dimensionless Hamaker constant (or drop size, $Ca_c \sim R^{-2/9}$) but a relatively strong function of the viscosity ratio, $Ca_c \sim \lambda^{-2/3}$.

4. RESULTS FOR GLANCING COLLISIONS

The simulations with a time independent external flow were performed to simulate interactions of drops during a head-on collision. However, at least from a practical point of view, the case of glancing collisions, where the drops rotate during the collision

process due to the initial offset from the inflow axis, is more important. In a glancing collision, the hydrodynamic force from the external flow along the line of centers changes with time, and there is a finite time available for film drainage before the drops eventually rotate to a configuration where they are separated by the flow. Thus, coalescence only occurs if Ca is smaller than some critical capillary number, Ca_c.

In this section, we consider "head-on" collisions in a time-dependent external flow, as a first step toward understanding glancing collisions. This is motivated by the earlier experimental study of Borrell *et al*. [12]. As explained earlier, this study shows that for the range of drop size and capillary number encompassed by our coalescence experiments ($R > 25$ μm and typical $Ca \leq O(10^{-3})$),that there is no measurable macroscopic difference in the drainage time prior to coalescence between a glancing collision and a head-on collision with the same history of force along the line of centers of drops. From these results we infer that the dynamics of film drainage are similar in the two experiments, suggesting that the glancing collision process can be described as the superposition of a translational motion along the line of centers plus a rotation of the line of centers relative to axes that are fixed in the flow for $Ca \ll 1$, as mentioned earlier. Specifically, the near axisymmetric film drainage process achieved in a head-on collision is apparently a good approximation of the same process in a non-axisymmetric glancing collision in 2D linear flow, which implies that the coalescence process is dominated by the time history of the force along the line of centers and is at least approximately independent of the degree of asymmetry in the overall collision process.

As in the Borrell *et. al*. [12] experiment, the rate of strain, $G(t)$, was chosen to mimic the time-dependence of the component of the force along the line of centers in

each particular glancing collision (i.e. for each offset, viscosity ratio and capillary number) between two spherical drops. As shown in Eqn. (1) – (3) of Borrell *et al*. [12], $G(t)$ can be related to the orientation angle θ for the line of centers between the drops in a glancing collision, according to

$$G(t) = G_0 \cos\left[2\theta(t)\right], \tag{49}$$

where G_0 is the strain rate based on a given capillary number (Ca_0), and θ is measured relative to the inflow symmetry axis of the 4-rol mill. Although the strain rate, G, is a function of time, the boundary-integral formulation, Eqn. (10), does not change. The capillary number for the undisturbed external flow in Eqn. (10) simply becomes a function of time

$$Ca = Ca_0\, \gamma(t), \tag{50}$$

where $Ca_0 = \mu_e G_0 R/\sigma$, and $\gamma(t) = \cos\left[2\theta(t)\right]$. The function $\theta(t)$ was determined from the theoretical prediction of the collision trajectory for two spherical drops, which previous studies in our group [7, 9] had shown to provide a very accurate prediction of the measured angle versus time, even for drops at finite G. The theoretical trajectory was calculated using the code from Tretheway *et al*. [7], based on the numerical scheme described in Yang *et al*. [9]. An example of the predicted and measured orientation angle versus time is shown in Fig. 23. It can be seen that the data and predictions are virtually identical. The initial offset is defined as the shortest distance from the center of the drop to the inflow axis, divided by R, at the center-to-center distance of $4R$ [9, 11].

We calculated the critical capillary number (Ca_c) and coalescence angle (i. e. time) at which coalescence occurs, for collisions in a time-dependent flow, at the two different

viscosity ratios of 0.19 and 1.2. The drop size is fixed as 27.2 μm, and the other parameters are the same as described earlier. The angle in this axisymmetric simulation is represented by the corresponding value of $\gamma(t) = \cos\left[2\theta(t)\right]$ at any instant.

4.1. Coalescence angle and thin film shape for λ = 0.19

Figure 24 shows the coalescence angle as a function of Ca at various initial offsets for $\lambda =$ 0.19 (again different offsets are represented by different dependences of θ on time). The largest value of Ca for each set of data corresponds to Ca_c. The critical capillary number decreases, and the maximum coalescence angle increases with increase of the offset. At the larger offsets from 0.14 – 0.17, coalescence occurs beyond 45°, after the external flow starts to pull the drops apart (i. e. $G < 0$). Above an initial offset of 0.17, coalescence is impossible. These results are qualitatively consistent with our experimental study of glancing collisions [11] (cf. Fig. 7 in Yoon *et al*. [11]).

An interesting point is that the maximum coalescence angles are relatively small ($\theta < 30^\circ$) for the smaller offsets. For these cases, coalescence occurs relatively early in the collision process although there is a whole range of angles (and time) remaining where the external flow still pushes the drops together ($G > 0$ for $\theta < 45^\circ$). This phenomenon is caused by relaxation of the dimple formed between the drops while the drops rotate through $\theta = 45^\circ$. Figure 25(a) shows the evolution of the thin film at the smallest offset of 0.01 for two values of the capillary number just below and above Ca_c ($Ca =$ 0.015 and 0.0151). The local minimum and center film thickness ($h_{\min}$ and h_{center}), and the radius of the dimple (a) are shown in the figure. The corresponding angle is also

plotted by a dotted line. When $Ca = 0.015$, coalescence occurs at $\theta = 26^\circ$. For the slightly increased capillary number of 0.0151, the local minimum film thickness is indistinguishable in Fig 25(a) over almost the complete trajectory, but deviates just prior to reaching $\theta = 26^\circ$, with a minimum film thickness that is slightly larger than the critical value occurring at around $\theta = 27^\circ$. The thin film shapes for Ca=0.0151 are shown in Fig 25(b) at the moments indicated in Fig. 25(a) by the open circles. It can be seen that the dimple begins to relax beginning approximately at $\theta = 27^\circ$ due to the decreasing hydrodynamic force from the external flow, and that it is the corresponding evolution of film shapes that cause the film thickness to exhibit a local minimum at this point in the trajectory. Further, by comparing 25(a) and 25(b) it is evident that there is a phase lag between the external force, which changes sign at $\theta = 45^\circ$, and the film shape, which still shows a significant dimple at that point. The dimple eventually disappears ($h_{\min} = h_{center}$) at around $\theta = 55^\circ$. As the drops are pulled apart, there is a "suction pressure" induced in the thin film. This causes a secondary minimum of the film thickness to appear at $\theta = 58^\circ$ as the interfaces to bulge toward each other near the line of centers right before the apparent separation of the drops. However, at this offset and viscosity ratio, the secondary minimum of the film thickness is much larger than the first minimum for $\theta < 45^\circ$ and cannot trigger film rupture.

When the offset is close to the maximum offset for coalescence, the local deformation of the thin film is quite different. Figure 26 shows the evolution of thin film for two values of *Ca* at the largest offset of 0.17. When $Ca = 0.0069$, the drops coalesce at about $\theta = 55^\circ$, after the force has changed sign ($G < 0$) and the drops are being pulled apart. When the initial offset is smaller, the drops collide more forcefully, and the thin

film becomes dimpled relatively early in the collision process, as shown earlier. In contrast, as the offset increases, the drops collide more gently. Eventually, above a certain offset, the thin film remains relatively spherical (or only has a very small dimple) during the early stage of the collision process ($\theta < 45^\circ$). Thus in this case, the interface thickness decreases continuously up to 45° as the drops move toward one another, and then continues to decrease beyond 45° as the interfaces bulge outward due to the "suction pressure". This local deformation induces the film to rupture, and the coalescence angle continuously increases beyond 45° as previously shown in the coalescence angle data in Fig. 24. For the slightly increased capillary number of 0.007, the interfaces are abruptly pulled inward to the center of the drops at around $\theta = 55^\circ$, and the drops separate as shown in Fig. 26. The important difference is that the local "suction" induced deformation starts to occur at around $\theta = 45^\circ$ for the larger offsets, whereas for the smaller offsets, this local deformation is retarded due to relaxation of the dimple, and starts to occur at a relatively larger angle after the dimple disappears, only a little before the apparent separation of the drops.

When $Ca > Ca_c$, the locally bulging interface causes a secondary (or primary for larger offsets) minimum in the film thickness at the angle of around 55° - 58°. Figure 27 shows the minimum of the film thickness for $\theta > 45^\circ$, caused by the locally bulging interface. The minimum of the film thickness decreases with the increase of the offset. However, all values of the film thickness are much larger than the critical film thickness found in the constant flow collision simulation ($h_c \cong 0.0004$, $h_c' \cong 100\,\text{Å}$ for $R =$ 27.2 μm), except in the case of the largest offset.

4.2. Coalescence angle and thin film shape for $\lambda = 1.2$

The coalescence angle as a function of Ca for the higher viscosity ratio of 1.2 is shown in Fig. 28. Qualitatively, the results look similar to the lower viscosity ratio. There are, however, several differences between the results for $\lambda = 0.19$ and 1.2. First of all, the critical capillary numbers are much smaller than those at the lower viscosity ratio, and the maximum offset for coalescence is also smaller. The maximum coalescence angles at the same initial offsets are also larger than in the case of the lower viscosity ratio. These results are again qualitatively consistent with our earlier experimental results for glancing collisions [11].

However, there are also significant differences between the experimental and simulation results. First, the experimental data (cf. Fig. 9 in Yoon *et al*. [11]) for offsets in the range 0.05 – 0.08 shows that the coalescence angle increases continuously with Ca up to a certain value, and then abruptly increases to around 58°. At the higher offsets (0.1 ≤ offset ≤ 0.12), the coalescence angle continuously increases with Ca up to around 58°, as also shown by the higher offset predictions in Fig. 28. However, in the experiments, the drops continue to coalesce over a significant range of capillary number with the coalescence angle fixed at about $\theta = 58^\circ$. In the simulations, there is a secondary minimum in the film thickness at $\theta = 58^\circ$ for the larger Ca values, but (unlike the experiments) the film thickness is not small enough to induce coalescence beyond the angles shown in Figure 28.

Figure 29 shows the evolution of the thin film at the lowest offset of 0.01 for $\lambda = 1.2$, again for two values of *Ca,* one above and one below Ca_c for this case. The evolution of

the thin film looks qualitatively similar to the case of $\lambda = 0.19$, as shown earlier in Fig. 25. The same types of data shown in Fig. 25 are also plotted in this figure. The dimple is smaller than for $\lambda = 0.19$ due to the smaller value of capillary number (or Ca_c), and the critical coalescence angle is larger due to the fact that the drainage process is slower because of the larger value of λ.

The evolution of the thin film at an "intermediate" offset of 0.06 for $\lambda = 1.2$ is shown in Fig. 30. This is one of the cases where the experiments showed a discontinuous transition from coalescence angles less than 45° to coalescence at angles at 58°. In the simulations, for $Ca = 0.00253$, coalescence occurs at $\theta = 45^\circ$. This is larger than the maximum angle prior to the jump in angles that was seen in the experiments, but this may be a consequence inadequate resolution in the experiments. Clearly, based on the results in Fig 28, the angle becomes extremely sensitive to Ca in this regime. When Ca is increased to 0.00254, however, coalescence is not predicted as observed for both the glancing and time-dependent flow experiments at $\theta = 58^\circ$. The computed results are qualitatively similar to those of the lower offset case (Fig 29), however, the dimple is smaller than in the lower offset case, and the dimple starts to relax at a larger angle. The "suction" induced local deformation, occurring right before the apparent separation of the drops, causes a secondary minimum of the film thickness at about $\theta = 58^\circ$, but cannot induce film rupture. Thus, the simulation does not predict the abrupt jump of the coalescence angle for $\lambda = 1.2$. However, the angle (or time) at which the secondary minimum occurs is exactly the same as the coalescence angle of the experiment. Furthermore, the relaxation of the dimple is completed at a much smaller film thickness than when the offset is 0.01, due to the smaller dimple formed in the early stage of the

collision process, and the secondary minimum film thickness is significantly smaller than when the offset is 0.01. However, for reasons that we do not currently understand, the simulated film thickness is still not small enough to produce coalescence even though this is observed in the experiments.

When the offset is close to the maximum offset for coalescence, the local deformation of the thin film is similar to the case of λ = 0.19. Figure 31 shows the evolution of the thin film for two values of *Ca* at the largest offset of 0.13. When *Ca* = 0.00257, coalescence occurs at $\theta = 58^{\circ}$, as the drops are being pulled apart. For the slightly increased capillary number of 0.00258, the drops separate at around $\theta = 58^{\circ}$. The local deformation for $\theta > 45^{\circ}$ is not caused by the van der Waals force even though this might seem an alternative explanation due to the small film thickness at $\theta = 45^{\circ}$. A comparison of the film evolution with and without the van der Waals force for the same capillary number (*Ca* = 0.00253) is shown in Fig. 32. The inset shows the film shapes for A_H = 0, at the moments indicated in the figure. Although the van der Waals force is not included, the local minimum film thickness still decreases due to the deformation mechanism mentioned above.

Figure 33 shows the minimum of the film thickness for $\theta > 45^{\circ}$ when $Ca > Ca_c$, caused by the locally bulging interface (λ =1.2). The results again qualitatively look similar to the lower viscosity ratio case, as shown in Fig. 27. However, there is one important difference. The secondary minimum film thickness is much smaller than that for λ = 0.19 at the same offset. This is caused by the fact that the local deformation is enhanced as the viscosity ratio increases, since the lubrication effect in the thin film becomes stronger. The force from the external flow that pulls the drops apart must

become strong enough to overcome the enhanced lubrication force, and this means that the "suction" pressures in the thin film are also enhanced prior to the drops separating.

It will be noted that some of the film thicknesses for the larger offsets are much smaller than the critical film thickness found in the time-independent flow collision simulation ($h_c \cong 0.0004$, $h_c' \cong 100\,\text{Å}$ for $R = 27.2$ μm), even though all the results in Fig 33 are for cases ($Ca > Ca_c$) where no coalescence is predicted. The fact that these films do not rupture is presumably due to a combination of the increased local curvature (and hence enhanced stabilization due to capillary forces) as well as the rapid transient nature of the film deformation process. Nevertheless, as already noted, coalescence is observed in the corresponding experiments.

4.3. Critical capillary number as a function of the initial offset

Figure 34 shows the critical capillary number as a function of the initial offset for the time-dependent flow simulations as well as the glancing collision experiment. Coalescence only occurs if Ca is smaller than Ca_c and the offset is smaller than the maximum offset. The results for the lower viscosity ratio of 0.19 look similar to each other although the critical capillary number and maximum offset are a little larger than measured in the experiment. On the other hand, the results for the higher viscosity ratio of 1.2 severely deviate at the larger offsets since the simulation is not able to predict the jump and plateau in the coalescence angle that is observed experimentally.

5. DISCUSSION

The current numerical simulations captured at least some of the mechanisms that are responsible for the complex behavior of coalescence for both head-on and glancing collisions outlined in our earlier experimental studies [9, 11, 12]. The simulations qualitatively predicted the head-on collision experimental results for the higher capillary numbers but not for the lower capillary numbers, where the thin film remains relatively spherical during the collision process. The drop size dependence of the drainage time was also weaker than in the experiments.

The time-dependent flow simulations only provided a quantitatively accurate description of the glancing collision experiments for the lowest viscosity ratio of 0.19. The results for coalescence angles less than 45° are similar to the experiments for $\lambda = 1.2$, and the results also confirm our earlier hypothesis of a minimum in the film thickness for an angle of approximately 58° due to a local outward bulging of the interfaces as the drops were being pulled apart. However, this local deformation did not trigger the film rupture at the smaller offsets, as observed in both the glancing and time-dependent flow collision experiments, nor did it reproduce the extended range of capillary numbers where coalescence was experimentally observed for the larger offsets.

There are a number of factors that could be responsible for the discrepancy between the simulation and experiments. We list some of these below, though we should emphasize that we do not currently know which (if any) is the critical issue.

First of all, in spite of the arguments at the beginning of this paper, it is possible that the assumption of axisymmetry may be partially responsible. The drops as well as the thin film are actually not axisymmetric in the applied two dimensional linear flow generated by the four-roll mill. The axisymmetric assumption is expected to be a good

approximation when $Ca \ll 1$, as mentioned earlier. We have also carried out a (as yet unpublished) [36] linear stability analysis of an axisymmetric thin film of finite radius equal to that in the coalescence problem to compare the conditions for instability to axisymmetric and non-axisymmetric perturbations of shape. This analysis shows that the conditions (film thickness) for instability are virtually the same, again supporting the relevance of the axisymmetric assumption for the present work. Finally, for many of the discrepancies between the simulations and the experiments, it unlikely that non-axisymmetric film shapes will play a role. This is particularly true of the differences in coalescence behavior for angles greater than 45°. Nevertheless, at this point, we cannot systematically quantify the difference in the thin film dynamics caused by the axisymmetric assumption.

The fluids used in the experiments are macroscopically Newtonian under the weak flow conditions of the experiments, but actually are polymers with moderate molecular weights. Polydimethylsiloxane (PDMS, M_n = 103,400) was used as the suspending fluid, and different molecular weights of polybutadiene (PBd, M_n = 5,000 – 24,900) were used as the drop to change the viscosity ratio from $O(0.1-10)$. Viscoelastic effects are negligible for the external flow, and negligible even for the drainage flow in the thin film, based upon estimates of the Deborah number the external shear rates and the shear rates that occur locally in the thin gap region during the drainage process. Viscoelastic effects will likely play a role in the final stages of film rupture, once the film is being rapidly thinned by van der Waals forces, but this will not have any significant effect on the quantities, such as drainage time, coalescence angle or critical capillary number that we are predicting. However, one place that viscoelastic effects may play a role is in the

predictions of coalescence (or no coalescence) due to the local "suction" induced deformation as the drops are being pulled apart. In this case, the length scales are small, and the interface deformation process is relatively rapid, suggesting that the enhanced extensional viscosity of the polymeric fluid could produce an increase in the interface deformation, and hence a decrease in the minimum film thickness. Although this effect will not be a large one, it may be sufficient to induce coalescence for cases where the simulations currently predict none. And it might be the reason why we observed the abrupt jump and the plateau in the coalescence angle in the experiments, but not in the simulations.

Finally, the continuum fluid mechanics framework may no longer be valid at some point, when the film thickness becomes very small. The calculated film thickness decreases way below 100 $\mathring{A}$ for some cases, depending on the parameters. This is only a factor of 6 – 8 larger than the radius of gyration of an entanglement segment in the PDMS. However, at this point, we do not know the limit. Also, in reality, the interface is not sharp but diffuse, with a finite transition region. The typical interfacial thickness can be as large as several nanometers for immiscible polymers ($\cong 50\,\mathring{A}$) [42-44]. If the mean film thickness becomes comparable to the interfacial thickness, the continuum theory will break down.

The van der Waals force is introduced in the boundary-integral formulation, using a disjoining pressure approximation, which is inversely proportional to the local film thickness ($\sim 1/h^3$). The disjoining pressure increases the dynamic pressure of the thin film near the region where the local minimum film thickness occurs, and this enhances the film drainage at this point once the van der Waals force becomes significant. This

approximate method has been used here, and is commonly adopted as a way to introduce the van der Waals force in the boundary integral method. However, the van der Waals force is induced by the interaction energy between the two bodies and depends on the geometries of the bodies. The disjoining pressure is only defined exactly as $p_{disj} \equiv A_H / 6\pi h^3$, for the interaction force per unit area between two infinite flat and sharp interfaces. Therefore, the disjoining pressure can provide a good leading order approximation for relatively flat interfaces ($\kappa \cong 0$), but will always fail to capture the physics involved in the final stages of film rupture, as the local curvature increases [45, 46], or as the film thickness decreases to the point that the diffuse nature of the interface can no longer be ignored. As shown earlier, the curvatures over the region where the actual film rupture occurs are $O(1)$ when the film thickness becomes comparable to the critical film thickness. Thus, there are serious issues about the use of the disjoining pressure approximation for the van der Waals force.

These and related questions are the subject of current investigations from our lab.

6. CONCLUSIONS

Numerical studies for the coalescence of two equal-sized deformable drops in an axisymmetric flow were performed using a boundary-integral method. An adaptive mesh refinement method was used to resolve the local small-scale dynamics in the gap and to retain a reasonable speed of computation. The thin film dynamics was successfully studied within a classical continuum mechanics framework, with sufficient stability and accuracy, up to a film thickness of $O(10^{-4})$ times undeformed drop radius, for a range of capillary numbers from $O(10^{-4} - 10^{-1})$ and viscosity ratios from $O(0.1 - 10)$. The results

were compared with the experimental data of our earlier studies [9, 11, 12] and provide good insight into the flow-induced coalescence process. The collisions for time-independent flow (termed "head-on" collisions in the experimental studies) showed two distinctively different regimes. At lower capillary numbers, the interfaces of thin film between the colliding drops remained almost spherical up to the point of film rupture, and the drainage time scaled as $t_d G \sim Ca$. In this case, the drainage time is relatively short because a steep pressure gradient is formed at the center of the film. The experiment, however, showed a plateau in the dependence of $t_d G$ on Ca. At higher capillary numbers, the film became dimpled at an early stage of the collision process, and the rate of the film drainage significantly slowed down after the dimple was fully formed. At this stage, the thin film pressure reaches the maximum value of the capillary pressure due to the deformation, with the pressure gradient only occurring near the rim of the dimple. In this case, the drainage time scaled approximately as $t_d G \sim Ca^{4/3}$, which is consistent with the experimental data as well as a slightly modified version of the existing scaling theory. Using the Hamaker constant calculated by the Lifshitz theory, the calculated drainage times showed quantitatively good agreements with the experimentally measured drainage time for $R = 27.2$ μm. However, the predicted drop size dependence of the drainage time was weaker than in the experiments. The critical conditions for coalescence were also examined when the internal circulation within the drop, induced by the outer flow, arrests the film drainage, and the results were consistent with the asymptotic analysis of Nemer *et al*. [20]. For the collisions in a time-dependent flow, which approximate coalescence in "glancing collisions", the simulations predicted many aspects of the experimental results. The results, however, were only quantitatively accurate, in comparison with the

experimental data, for the lowest viscosity ratio of 0.19. The interfaces of the thin film locally bulged outward when the drops were being pulled apart ($\theta > 45^\circ$ or $G < 0$), as previously hypothesized. This local deformation caused a secondary (or primary for larger offsets) minimum in the film thickness for $\theta \approx 55 - 58^\circ$, when $Ca > Ca_c$. The local deformation started to occur at around $\theta = 45^\circ$ for the larger offsets. For the smaller offsets, however, the local deformation was retarded, due to the relaxation of the dimple, and occurred at a relatively larger angle after the dimple disappeared, a little before the apparent separation of the drops in the flow. Thus, at the larger offsets, the coalescence angle continuously increases with Ca up to the separation angle, for $Ca < Ca_c$. At smaller offsets, however, the local deformation could not induce film rupture, as was observed in both the glancing and time-dependent flow collision experiments for the higher viscosity ratios. Therefore, the simulations predicted neither the abrupt jump nor the plateau of the coalescence angle for λ=1.2. We discussed some of the limitations of the current numerical study in interpreting the real coalescence problem. These and related questions will be the subject of continued investigation.

ACKNOWLEDGMENTS

The work of Yosang Yoon and Fabio Baldessari was supported by the Materials Science and Engineering Center at UCSB; L. Gary Leal was supported by a grant DE-F602-05ER25704 from Multiscale Mathematics and Science Program of the DOE; Hector Ceniceros was supported by a grant DMS 0609996 from the NSF .

REFERENCES

1. G. I. Taylor, "The viscosity of a fluid containing small drops of another fluid," Proc. R. Soc. London, Ser. A, **138**, 41-48 (1932).
2. G. I. Taylor, "The formation of emulsions in definable fields of flow," Proc. R. Soc. London, Ser. A, **146**, 501-523 (1934).
3. G. K. Youngren and A. Acrivos, "Shape of a Gas Bubble in a Viscous Extensional Flow," Journal of Fluid Mechanics, **76**, 433-442 (1976).
4. J. M. Rallison and A. Acrivos, "Numerical Study of Deformation and Burst of a Viscous Drop in an Extensional Flow," Journal of Fluid Mechanics, **89**, 191-200 (1978).
5. H. A. Stone, "Dynamics of drop deformation and breakup in viscous fluids," Annual Review of Fluid Mechanics, **26**, 65-102 (1994).
6. S. Guido and M. Simeone, "Binary collision of drops in simple shear flow by computer- assisted video optical microscopy," Journal of Fluid Mechanics, **357**, 1-20 (1998).
7. D. C. Tretheway, M. Muraoka, and L. G. Leal, "Experimental trajectories of two drops in planar extensional flow," Physics of Fluids, **11**, 971-981 (1999).
8. Y. T. Hu, D. J. Pine, and L. G. Leal, "Drop deformation, breakup, and coalescence with compatibilizer," Physics of Fluids, **12**, 484-489 (2000).
9. H. Yang, C. C. Park, Y. T. Hu, and L. G. Leal, "The coalescence of two equal-sized drops in a two-dimensional linear flow," Physics of Fluids, **13**, 1087-1106 (2001).
10. J. W. Ha, Y. Yoon, and L. G. Leal, "The effect of compatibilizer on the coalescence of two drops in flow," Physics of Fluids, **15**, 849-867 (2003).
11. Y. Yoon, M. Borrell, C. C. Park, and L. G. Leal, "Viscosity ratio effects on the coalescence of two equal-sized drops in a two-dimensional linear flow," Journal of Fluid Mechanics, **525**, 355-379 (2005).
12. M. Borrell, Y. Yoon, and L. G. Leal, "Experimental analysis of the coalescence process via head-on collisions in a time-dependent flow," Physics of Fluids, **16**, 3945-3954 (2004).
13. S. G. Yiantsios and R. H. Davis, "Close Approach and Deformation of 2 Viscous Drops Due to Gravity and Vanderwaals Forces," Journal of Colloid and Interface Science, **144**, 412-433 (1991).
14. S. Abid and A. K. Chesters, "The Drainage and Rupture of Partially-Mobile Films between Colliding Drops at Constant Approach Velocity," International Journal of Multiphase Flow, **20**, 613-629 (1994).
15. M. A. Rother, A. Z. Zinchenko, and R. H. Davis, "Buoyancy-driven coalescence of slightly deformable drops," Journal of Fluid Mechanics, **346**, 117-148 (1997).
16. A. K. Chesters and I. B. Bazhlekov, "Effect of insoluble surfactants on drainage and rupture of a film between drops interacting under a constant force," Journal of Colloid and Interface Science, **230**, 229-243 (2000).
17. I. B. Bazhlekov, A. K. Chesters, and F. N. van de Vosse, "The effect of the dispersed to continuous-phase viscosity ratio on film drainage between interacting drops," International Journal of Multiphase Flow, **26**, 445-466 (2000).

18. F. Baldessari and L. G. Leal, "Effect of overall drop deformation on flow-induced coalescence at low capillary numbers," Physics of Fluids, **18**, 3-90 (2006).
19. V. Cristini, J. Blawzdziewicz, and M. Loewenberg, "An adaptive mesh algorithm for evolving surfaces: Simulations of drop breakup and coalescence," Journal of Computational Physics, **168**, 445-463 (2001).
20. M. B. Nemer, et al., "Hindered and enhanced coalescence of drops in Stokes flows," Physical Review Letters, **92**, (2004).
21. M. Loewenberg and E. J. Hinch, "Numerical simulation of a concentrated emulsion in shear flow," Journal of Fluid Mechanics, **321**, 395-419 (1996).
22. M. Loewenberg and E. J. Hinch, "Collision of two deformable drops in shear flow," Journal of Fluid Mechanics, **338**, 299-315 (1997).
23. A. Z. Zinchenko, M. A. Rother, and R. H. Davis, "A novel boundary-integral algorithm for viscous interaction of deformable drops," Physics of Fluids, **9**, 1493-1511 (1997).
24. M. A. Rother and R. H. Davis, "The effect of slight deformation on droplet coalescence in linear flows," Physics of Fluids, **13**, 1178-1190 (2001).
25. A. K. Chesters, "The Modeling of Coalescence Processes in Fluid Liquid Dispersions - a Review of Current Understanding," Chemical Engineering Research & Design, **69**, 259-270 (1991).
26. R. H. Davis, "Buoyancy-driven viscous interaction of a rising drop with a smaller trailing drop," Physics of Fluids, **11**, 1016-1028 (1999).
27. C. Pozrikidis, *Boundary integral and singularity methods for linearized viscous flow*. Cambrige texts in applied mathematics. 1992, New York: Cambrige University Press.
28. W. B. Russel, D. A. Saville, and W. R. Schowalter, *Colloidal Dispersions*. 1989, Cambrige: Cambrige University Press.
29. S. Kim and S. Karilla, *Microhydrodynamics: Principles and Selected Applications*. 1991, Boston: Buttertworth-Heineman.
30. M. Abramowitz and I. A. Stegun, *Handbook of Mathematical Functions*. 1972, New York: Dover.
31. S. H. Lee and L. G. Leal, "The Motion of a Sphere in the Presence of a Deformable Interface .2. A Numerical Study of the Translation of a Sphere Normal to an Interface," Journal of Colloid and Interface Science, **87**, 81-106 (1982).
32. T. Y. Hou, J. S. Lowengrub, and M. J. Shelley, "Removing the Stiffness from Interfacial Flow with Surface-Tension," Journal of Computational Physics, **114**, 312-338 (1994).
33. T. Y. Hou, J. S. Lowengrub, and M. J. Shelley, "The long-time motion of vortex sheets with surface tension," Physics of Fluids, **9**, 1933-1954 (1997).
34. T. Y. Hou, J. S. Lowengrub, and M. J. Shelley, "Boundary integral methods for multicomponent fluids and multiphase materials," Journal of Computational Physics, **169**, 302-362 (2001).
35. H. D. Ceniceros and T. Y. Hou, "Convergence of a non-stiff boundary integral method for interfacial flows with surface tension," Mathemactics of Computation, **67**, 137-182 (1998).

36. F. Baldessari, *Theoretical studies of flow induced coalescence*, in *Chemical Engineering*. 2004, University of California: Santa Barbara.
37. J. M. Rallison, "A Numerical Study of the Deformation and Burst of a Viscous Drop in General Shear Flows," Journal of Fluid Mechanics, **109**, 465-482 (1981).
38. J. Israelachvili, *Intermolecular & Surface Forces*. 2 ed. 1991, San Diego: ACADEMIC PRESS.
39. C. C. Park, F. Baldessari, and L. G. Leal, "Study of molecular weight effects on coalescence: Interface slip layer," Journal of Rheology, **47**, 911-942 (2003).
40. G. K. Batchelor and J. T. Green, "Hydrodynamic Interaction of 2 Small Freely-Moving Spheres in a Linear Flow Field," Journal of Fluid Mechanics, **56**, 375-& (1972).
41. H. Wang, A. Z. Zinchenko, and R. H. Davis, "The Collision Rate of Small Drops in Linear Flow-Fields," Journal of Fluid Mechanics, **265**, 161-188 (1994).
42. E. Helfand and Y. Tagami, "Theory of Interface between Immiscible Polymers," Journal of Polymer Science Part B-Polymer Letters, **9**, 741-& (1971).
43. P. Perrin and R. E. Prudhomme, "Saxs Measurements of Interfacial Thickness in Amorphous Polymer Blends Containing a Diblock Copolymer," Macromolecules, **27**, 1852-1860 (1994).
44. G. D. Merfeld, et al., "Interfacial thickness in bilayers of poly(phenylene oxide) and styrenic copolymers," Journal of Polymer Science Part B-Polymer Physics, **36**, 3115-3125 (1998).
45. C. Maldarelli and R. K. Jain, "The Linear, Hydrodynamic Stability of an Interfacially Perturbed, Transversely Isotropic, Thin, Planar Viscoelastic Film .1. General Formulation and a Derivation of the Dispersion-Equation," Journal of Colloid and Interface Science, **90**, 233-262 (1982).
46. P. A. Kralchevsky and I. B. Ivanov, "Micromechanical Description of Curved Interfaces, Thin-Films, and Membranes .2. Film Surface Tensions, Disjoining Pressure and Interfacial Stress Balances," Journal of Colloid and Interface Science, **137**, 234-252 (1990).

List of figures

Figure 8. Evolution of the film shape for Ca = 0.0008, λ = 0.19, and A^* = 4.99×10^{-11}: (a) $h_{\min}$, h_{center}, and the radius of the thin film, a, as function of time; data without the van der Waals force ($A_H = 0$) are also presented by dotted lines; (b) thin film shapes at the moments indicated in Fig. 7(a) by the open circles.

Figure 9. Mean curvatures for the entire drop for Ca = 0.0008, λ = 0.19, and A^* = 4.99×10^{-11} at the moments indicated earlier in Fig. 8. Insect shows the curvature at $d = 2R$ (3rd plot in the main figure).

Figure 10. Drainage time as a function of Ca for R = 27.2 μm. The data of the simulations and experiments are shown by the solid symbols and open symbols respectively. The drainage times are scaled by the radius of drop for the comparison with the experiments.

Figure 11. Initial film thickness, h_0, when $d = 2R$, as a function of Ca.

Figure 12. Lateral extent of the dimpled region, a, as a function of Ca.

Figure 13. Film thickness, h_{dimple}, at which the dimple starts to form as a function of Ca

Figure 14. Drainage time as a function of viscosity ratio for R = 27.2 μm and Ca = 0.004.

Figure 15. Drainage time as a function of Ca for various values of the dimensionless Hamaker constant at λ = 0.19. The experimental data are also presented by solid triangles for R = 27.2 μm, solid circles for R = 40.1 μm, and solid squares for R = 45.4 μm.

Figure 16. Drainage time as a function of Ca for various values of the dimensionless Hamaker constant at λ = 1.2. The experimental data are also presented by solid triangles for R = 27.2 μm, solid circles for R = 35.6 μm, and solid squares for R = 44.7 μm.

Figure 17. Drainage time as a function of Ca for various values of the dimensionless Hamaker constant at $\lambda = 6.8$. The experimental data are also presented by solid triangles for $R = 27.2$ μm and solid circles for $R = 39$ μm.

Figure 18. Critical film thickness for coalescence as a function of λ at $Ca = 0.008$.

Figure 19. Critical film thickness for coalescence as a function of Ca for $\lambda = 0.19$.

Figure 20. Critical film thickness for coalescence as a function of the dimensionless Hamaker constant.

Figure 21. Evolution of the film shape for the two capillary numbers below and above the critical value at $A^* = 3.93\times10^{-9}$ and $\lambda = 1.2$. Insets show the stationary drop shape and the film profile for $Ca = 0.055$ at $tG = 100$.

Figure 22. Critical capillary number for head-on collision as a function of the dimensionless Hamaker constant.

Figure 23. Comparison of typical experimental and theoretical trajectories for $\lambda = 1.2$. The capillary number is slightly higher than Ca_c ($Ca = 0.00497$ for offset = 0.02, $Ca = 0.00433$ for offset = 0.06, $Ca = 0.00481$ for offset = 0.12).

Figure 24. Coalescence angle as a function of Ca for collisions in a time-dependent flow at several initial offsets, $\lambda = 0.19$, and $A^* = 4.99\times10^{-11}$.

Figure 25. Evolution of the film shape for offset = 0.01, $\lambda = 0.19$ and $A^* = 4.99\times10^{-11}$: (a) $h_{\min}$, h_{center}, and the radius of the dimple, a, as a function of time; (b) thin film shapes at the moments indicated by open circles in figure(a) for $Ca = 0.0151$.

Figure 26. Evolution of the film shape for offset = 0.17, $\lambda = 0.19$ and $A^* = 4.99\times10^{-11}$: (a) $h_{\min}$, h_{center}, and the radius of the dimple, a, as a function of time; (b) thin film shapes at the moments indicated by open circles in figure(a) for $Ca = 0.007$.

Figure 27. Secondary minimum of the film thickness for $\theta > 45^\circ$, when $Ca > Ca_c$ ($\lambda =$ 0.19).

Figure 28. Coalescence angle as a function of Ca for collisions in a time-dependent flow at several initial offsets, $\lambda = 1.2$, and $A^* = 4.78\times10^{-11}$.

Figure 29. Evolution of the film shape for offset = 0.01, $\lambda = 1.2$ and $A^* = 4.78\times10^{-11}$: (a) $h_{\min}$, h_{center}, and the radius of the dimple, a, as a function of time; (b) thin film shapes at the points indicated by open circles in figure(a) for $Ca = 0.00431$.

Figure 30. Evolution of the film shape for offset = 0.06, $\lambda = 1.2$ and $A^* = 4.78\times10^{-11}$: (a) $h_{\min}$, h_{center}, and the radius of the dimple, a, as a function of time; (b) thin film shapes at the points indicated by open circles in figure(a) for $Ca = 0.00254$.

Figure 31. Evolution of the film shape for offset = 0.13, $\lambda = 1.2$ and $A^* = 4.78\times10^{-11}$: (a) $h_{\min}$, h_{center}, and the radius of the dimple, a, as a function of time; (b) thin film shapes at the points indicated by open circles in figure(a) for $Ca = 0.00258$.

Figure 32. The comparison of the film evolutions with and without the van der Waals force for $Ca = 0.00253$. Inset shows the film shapes for $A_H = 0$ at the moments indicated in the figure.

Figure 33. Secondary minimum of the film thickness for $\theta > 45^\circ$, when $Ca > Ca_c$ ($\lambda =$ 0.19).

Figure 34. Critical capillary number as a function of the initial offset for the time-dependent flow simulation as well as the glancing collision experiment.

Table 1. Convergence of the coalescence time. The relative error is based on the result of step 3.

	n	Δs	# interpolation	tG_{coal}	Rel. error (%)
Uniform 1	500	0.0063	-	3.0458	41.8
Uniform 2	1000	0.0032	-	2.7201	26.6
Step 1	318	0.002	1	2.4641	14.7
Step 2	456	0.001	1	2.1951	2.18
Step 3	806	0.0005	1	2.1489	-
Adaptive 1	486	0.0005	7	2.1553	0.30
Adaptive 2	714	0.0003	9	2.1567	0.36

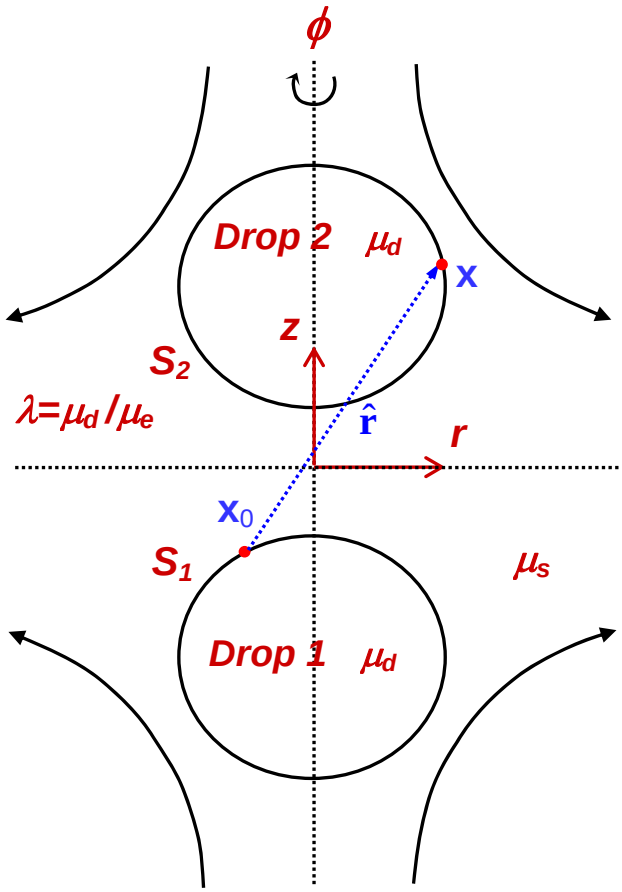

Figure 1. Schematic of two deformable drops in a linear axisymmetric flow.

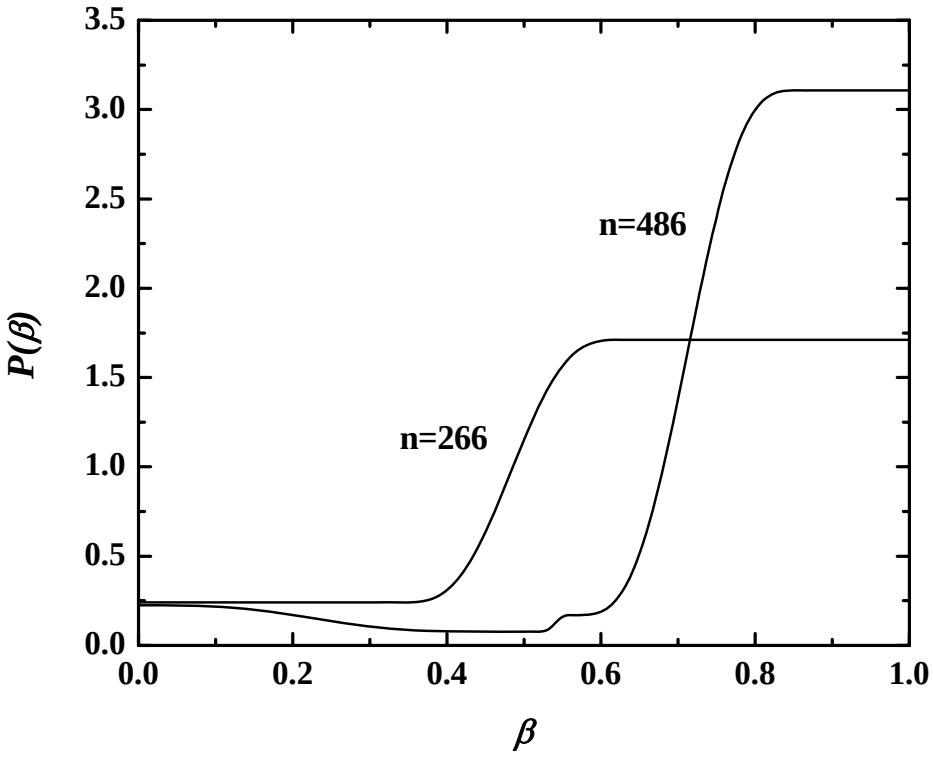

Figure 2. Typical examples of the node distribution function, $P(\beta)$, for non-uniform mesh.

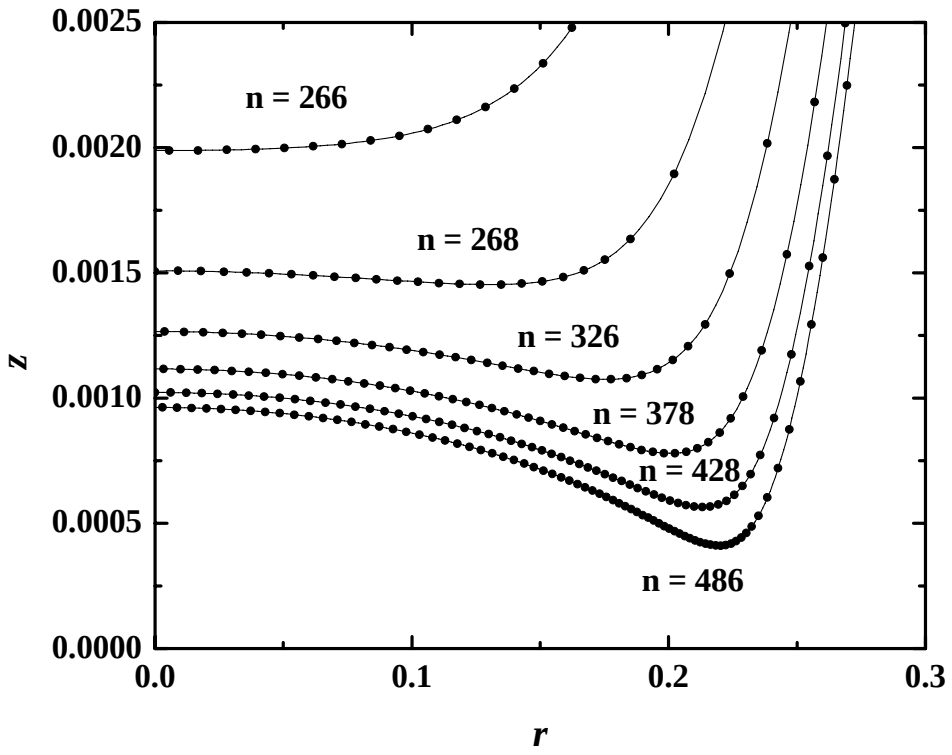

Figure 3. Evolution of the interface shape in the gap region as well as the node distribution for Ca = 0.015 and λ =0.19. The nodes are plotted every 4 points in the figure.

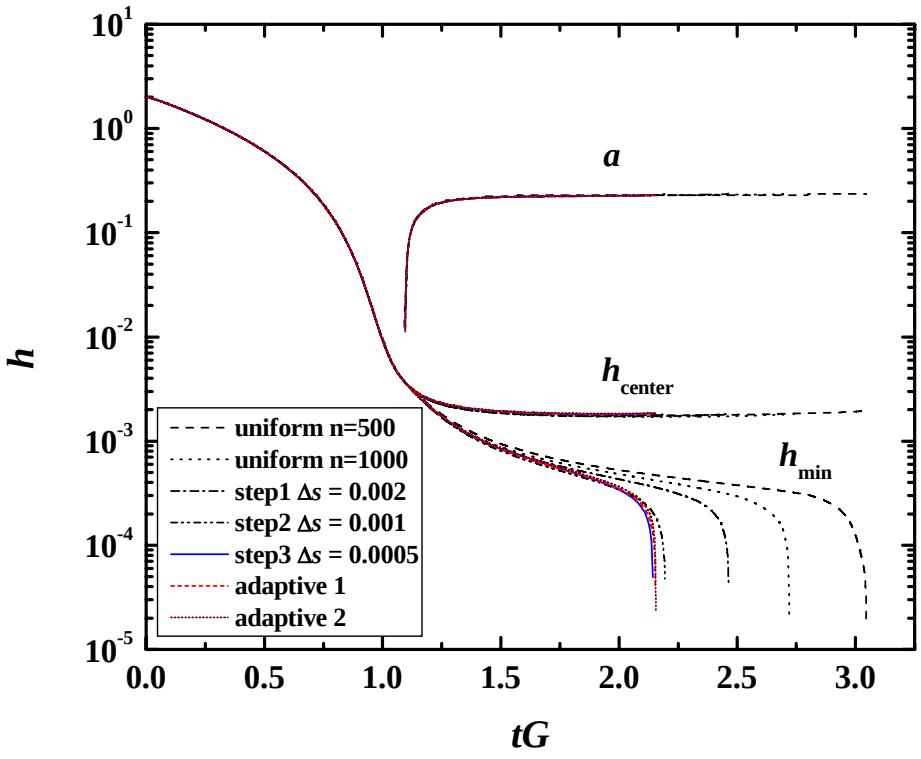

Figure 4. Evolution of the thin film calculated with varying node spacing for $Ca = 0.015$, $\lambda = 0.19$, and $A^* = 4.99\times10^{-11}$ ($R = 27.2$ μm and $\sigma = 4.6$mN/m): the local minimum film thickness, $h_{\min}$, the film thickness at the center of the film, h_{center}, and the radius of the thin film (or dimple), a as a function of time.

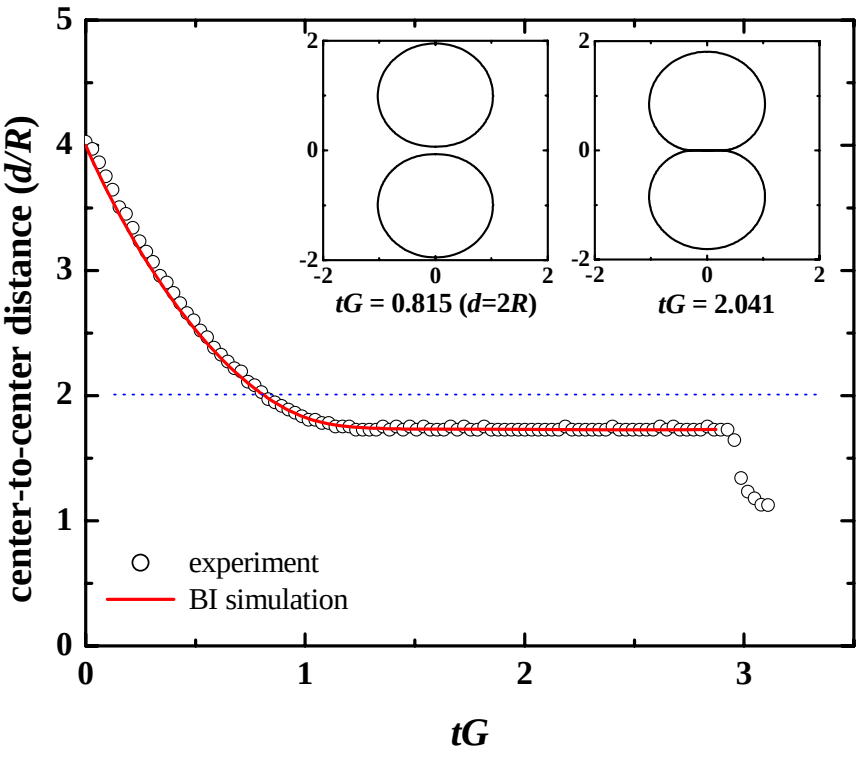

Figure 5. Comparison between the experimentally measured and the calculated center-to-center distance (d/R) as a function of dimensionless time (tG) for Ca = 0.0207, λ = 0.19, and A^* = 4.99×10^{-11} (R = 27.2 μm and σ = 4.6mN/m).

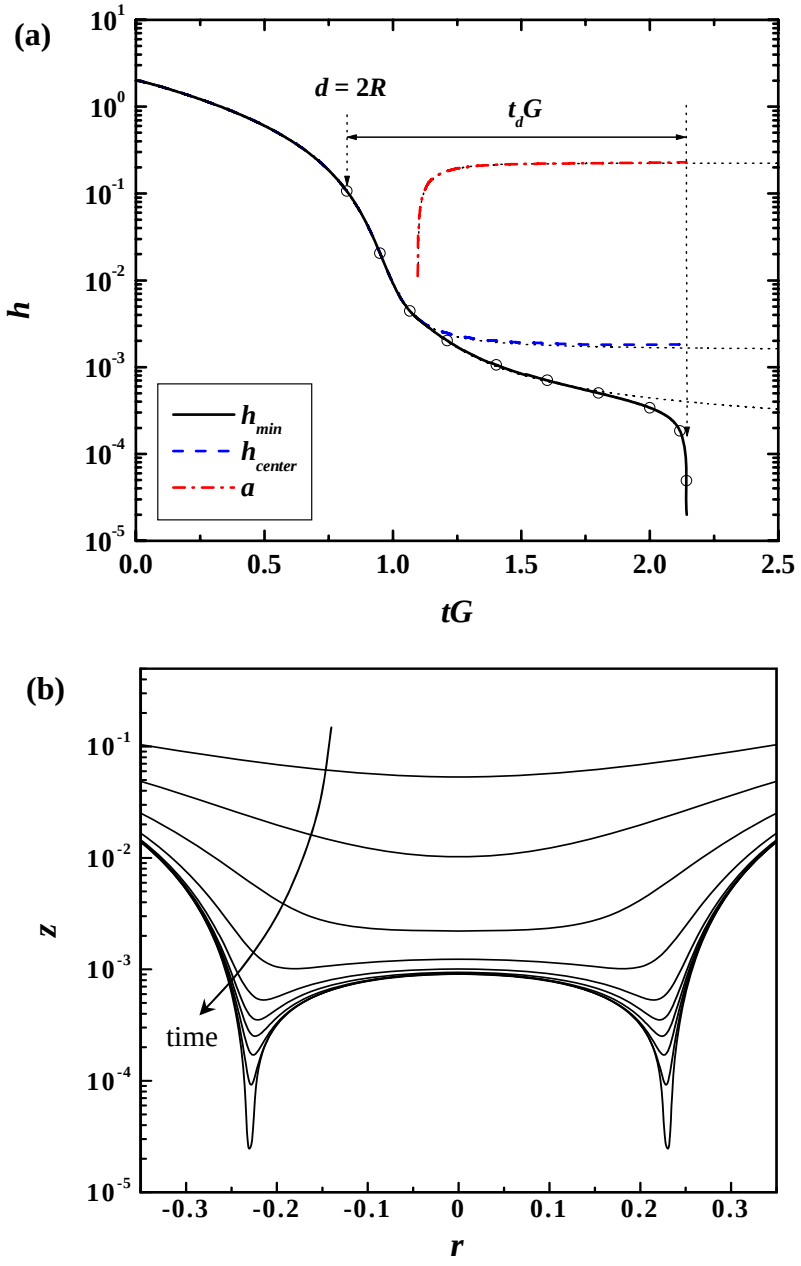

Figure 6. Evolution of the film shape for $Ca = 0.015$, $\lambda = 0.19$, and $A^* = 4.99\times10^{-11}$: (a) $h_{\min}$, h_{center}, and the radius of the thin film, a, as function of time; data without the van der Waals force ($A_H = 0$) are also presented by dotted lines; (b) thin film shapes at the moments indicated in Fig. 6(a) by the open circles.

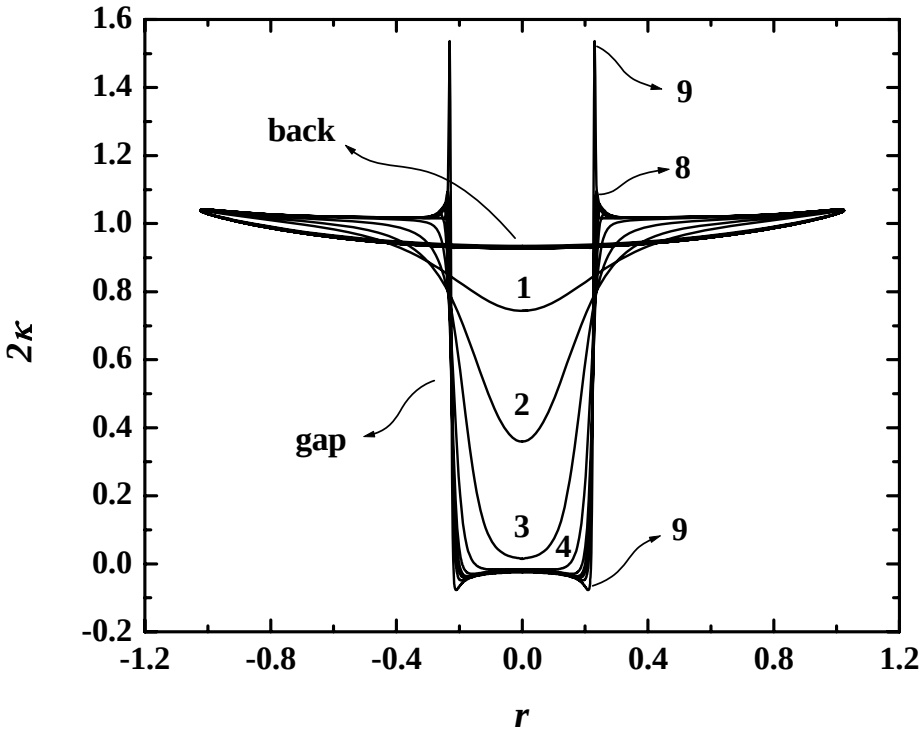

Figure 7. Mean curvatures for the entire drop for Ca = 0.015, λ = 0.19, and A^* = 4.99×10^{-11} at the moments indicated earlier in Fig. 6.

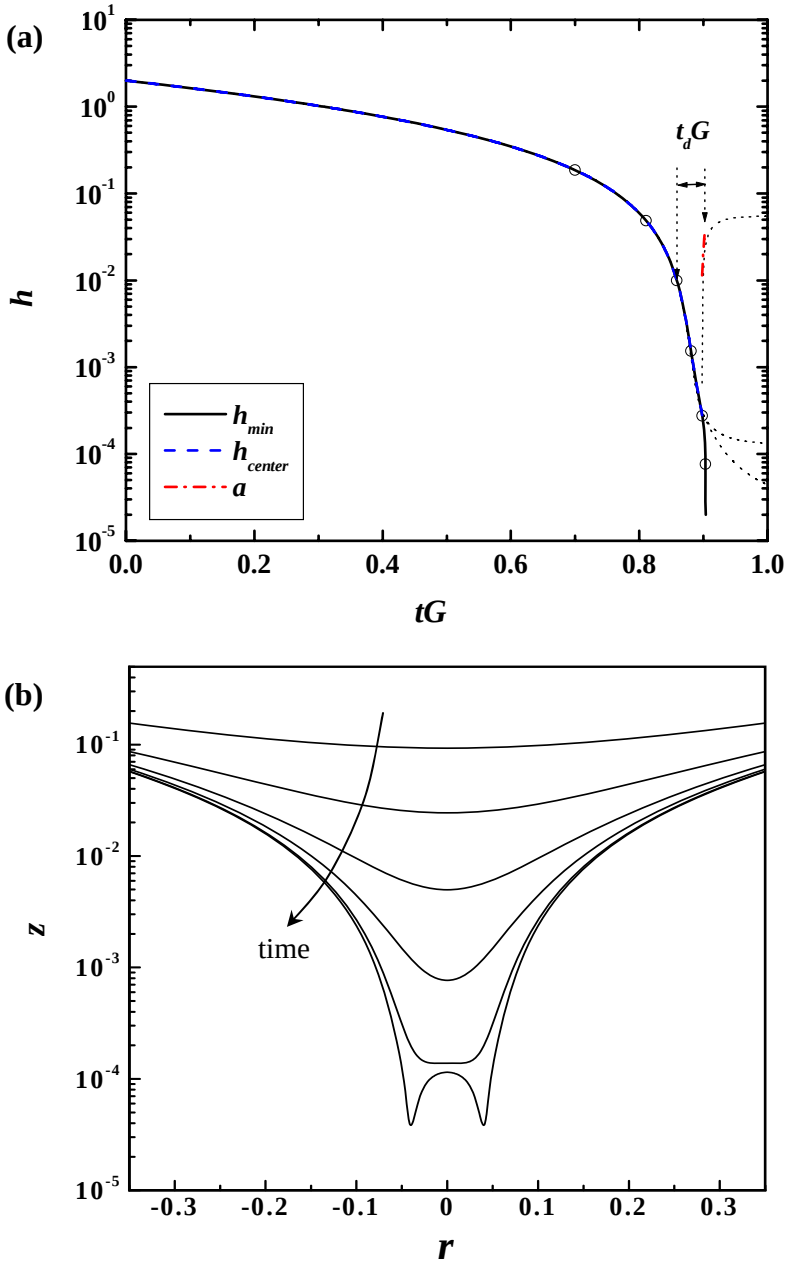

Figure 8. Evolution of the film shape for $Ca = 0.0008$, $\lambda = 0.19$, and $A^* = 4.99\times10^{-11}$: (a) $h_{\min}$, h_{center}, and the radius of the thin film, a, as function of time; data without the van der Waals force ($A_H = 0$) are also presented by dotted lines; (b) thin film shapes at the moments indicated in Fig. 7(a) by the open circles.

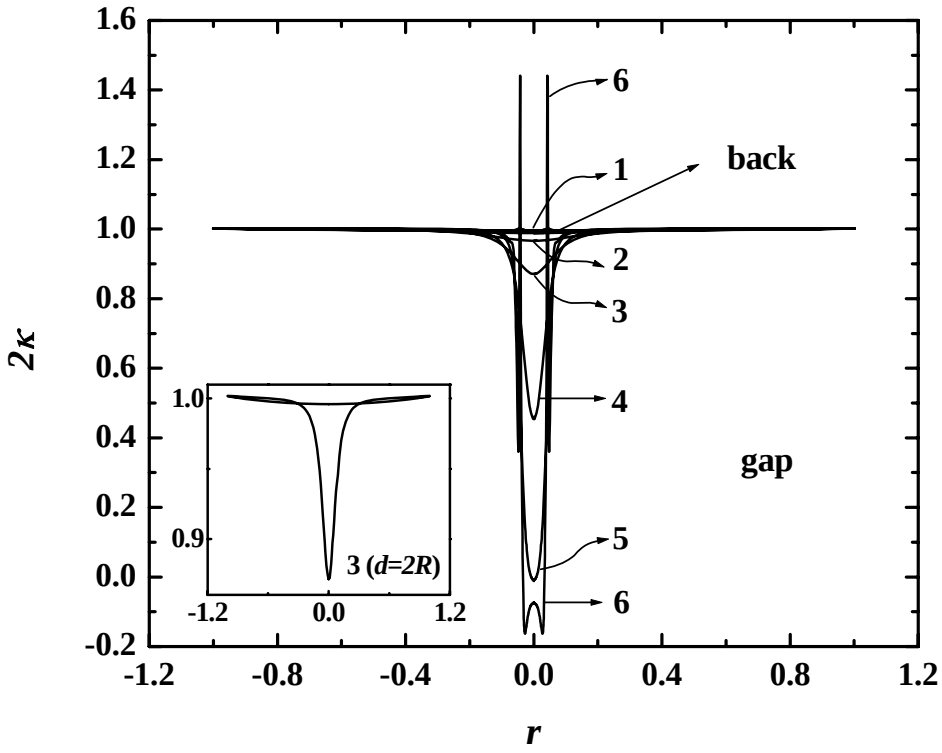

Figure 9. Mean curvatures for the entire drop for Ca = 0.0008, λ = 0.19, and A^* = 4.99×10^{-11} at the moments indicated earlier in Fig. 8. Insect shows the curvature at $d = 2R$ (3rd plot in the main figure).

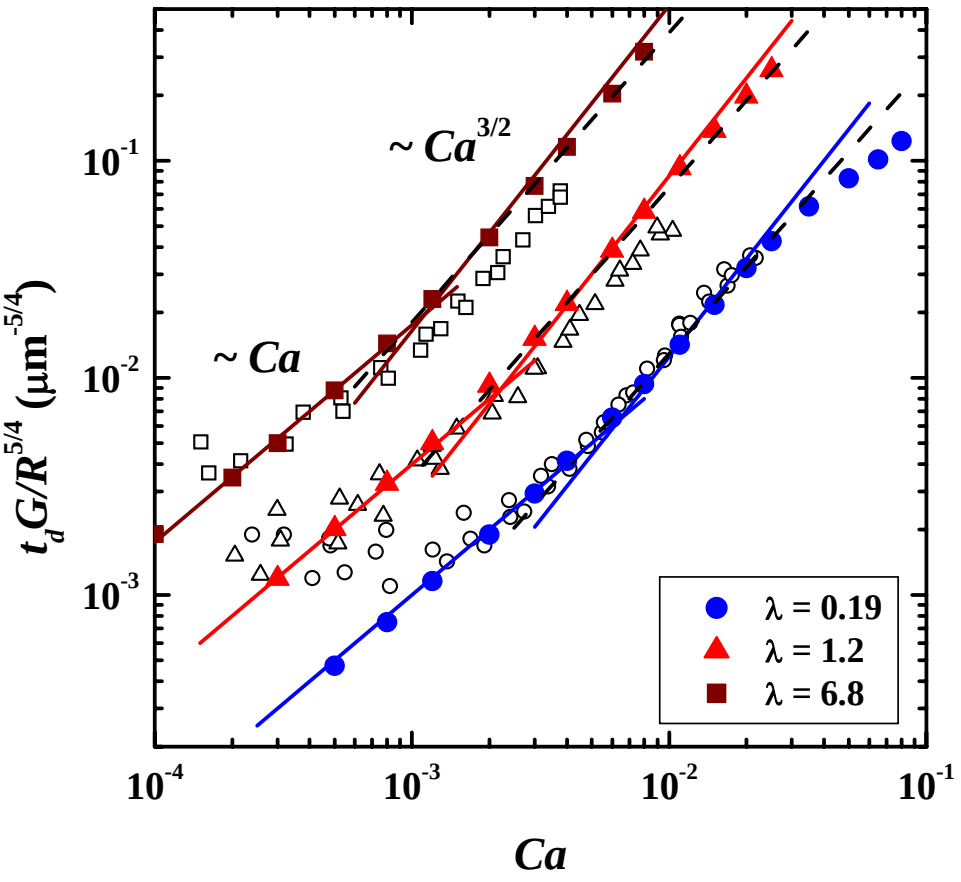

Figure 10. Drainage time as a function of *Ca* for R = 27.2 μm. The data of the simulations and experiments are shown by the solid symbols and open symbols respectively. The drainage times are scaled by the radius of drop for the comparison with the experiments.

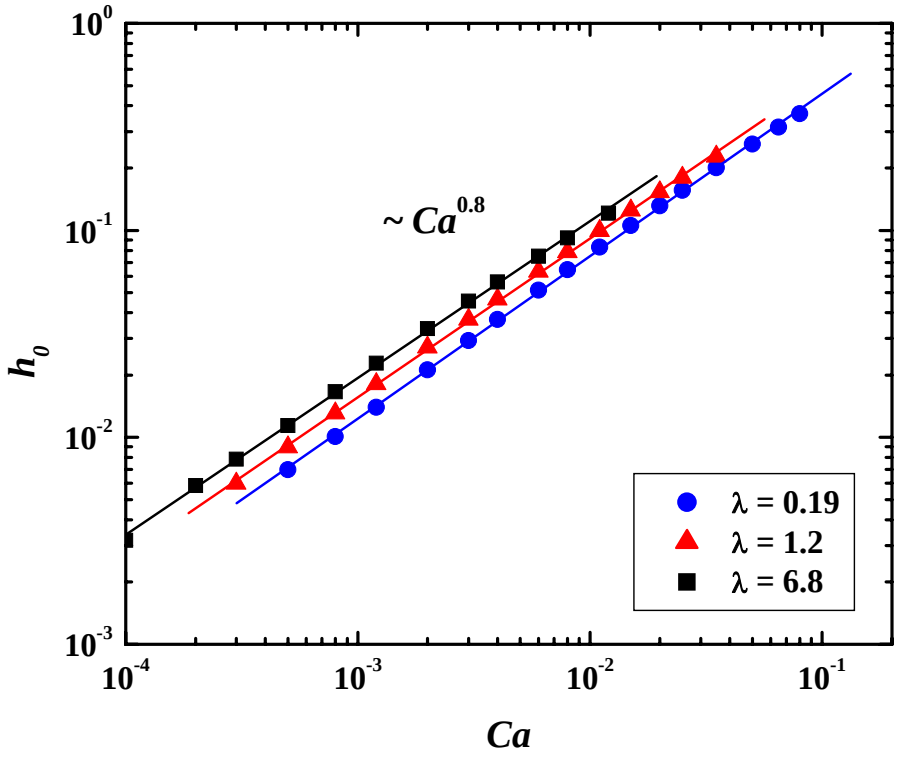

Figure 11. Initial film thickness, h_0, when $d = 2R$, as a function of Ca.

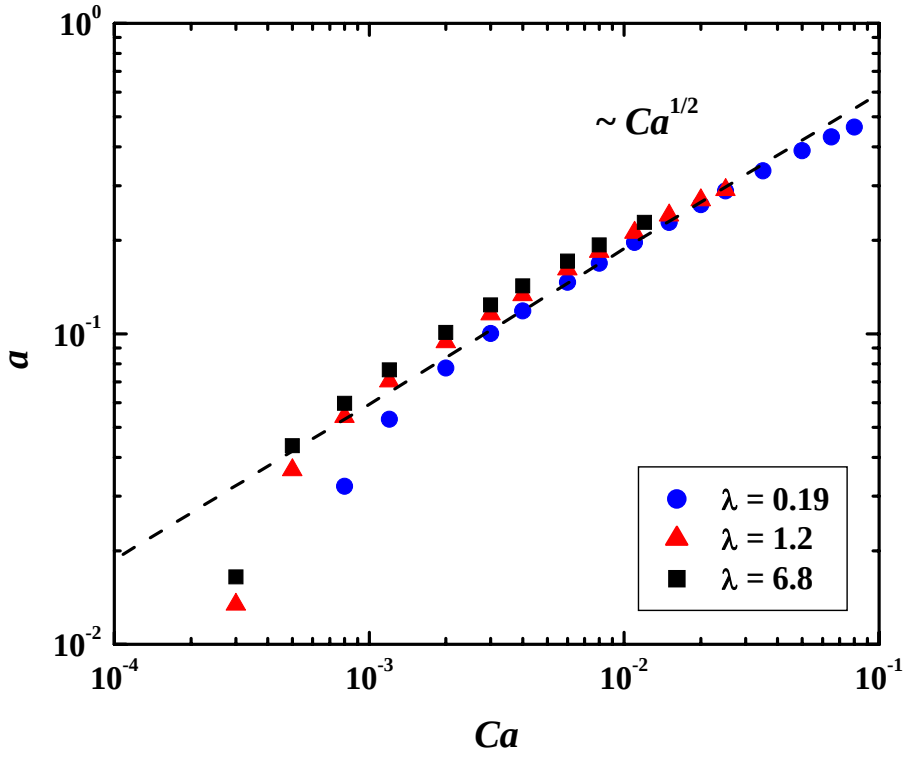

Figure 12. Lateral extent of the dimpled region, a, as a function of Ca.

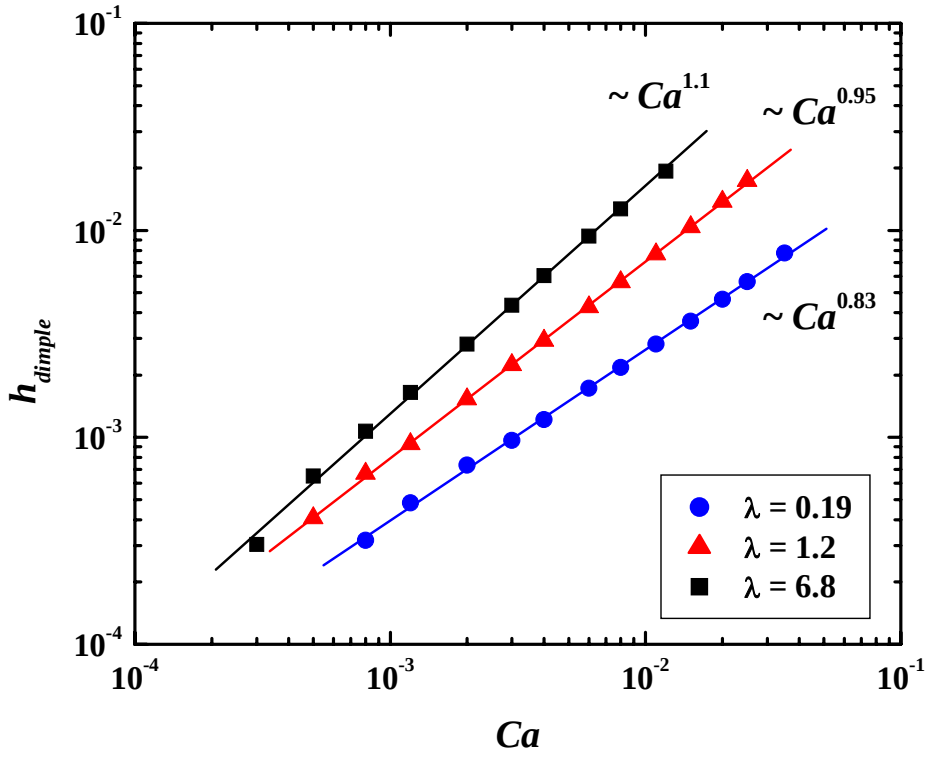

Figure 13. Film thickness, h_{dimple}, at which the dimple starts to form as a function of Ca

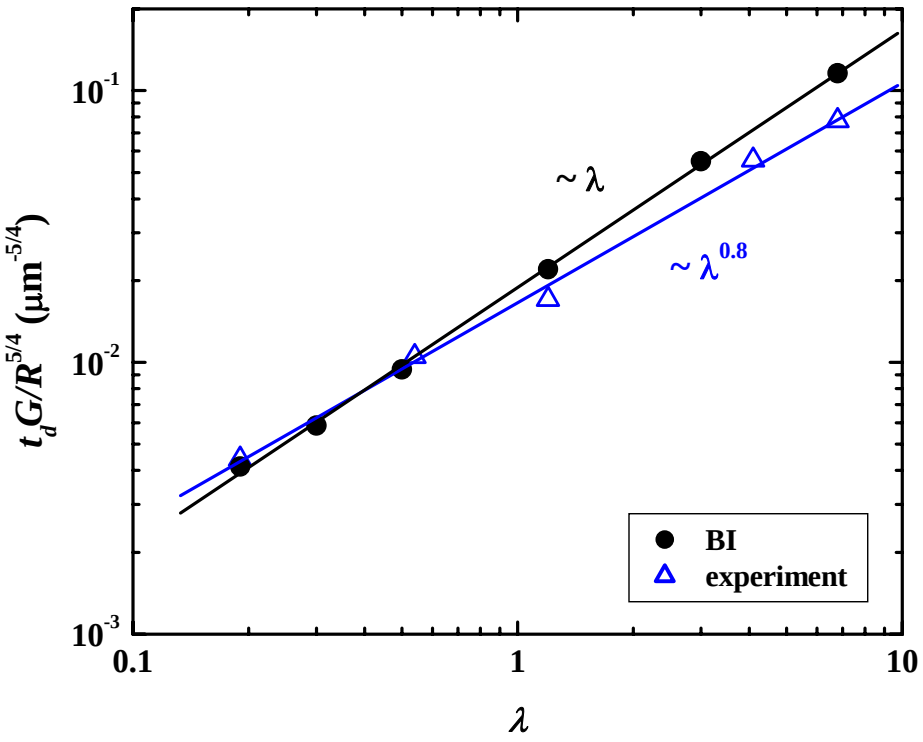

Figure 14. Drainage time as a function of viscosity ratio for R = 27.2 μm and Ca = 0.004.

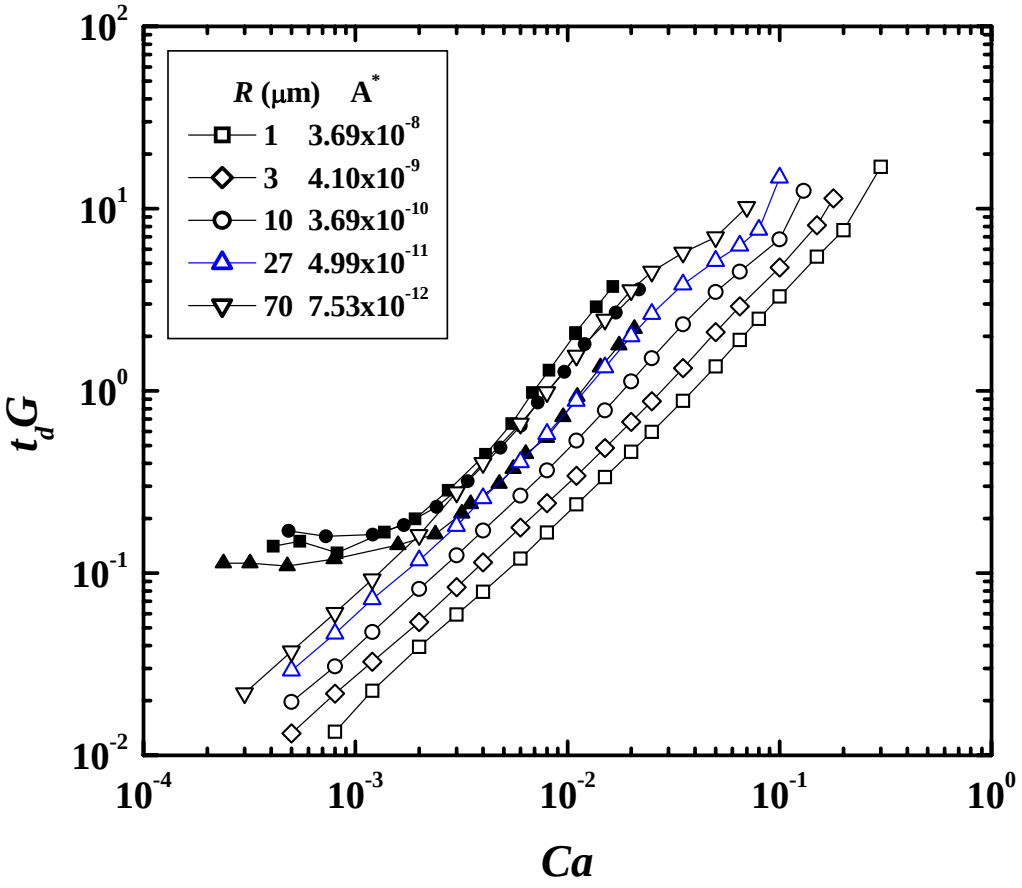

Figure 15. Drainage time as a function of *Ca* for various values of the dimensionless Hamaker constant at $\lambda = 0.19$. The experimental data are also presented by solid triangles for $R = 27.2$ μm, solid circles for $R = 40.1$ μm, and solid squares for $R = 45.4$ μm.

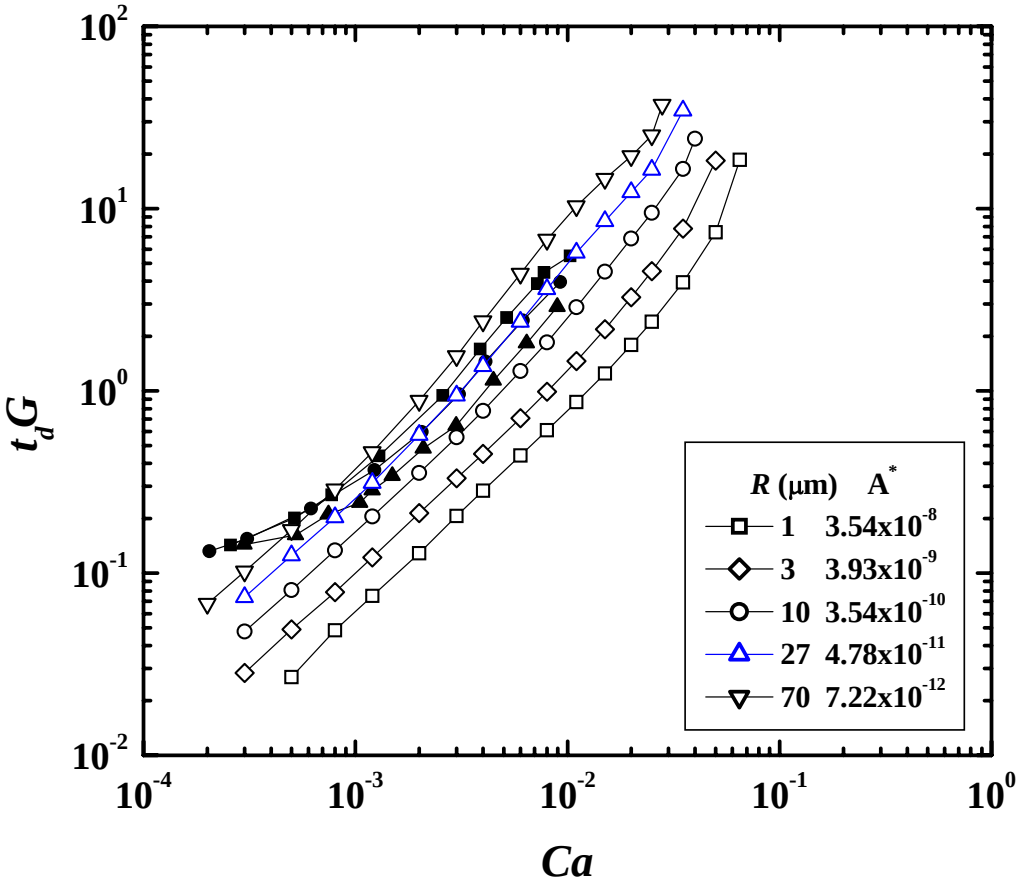

Figure 16. Drainage time as a function of *Ca* for various values of the dimensionless Hamaker constant at $\lambda = 1.2$. The experimental data are also presented by solid triangles for $R = 27.2$ μm, solid circles for $R = 35.6$ μm, and solid squares for $R = 44.7$ μm.

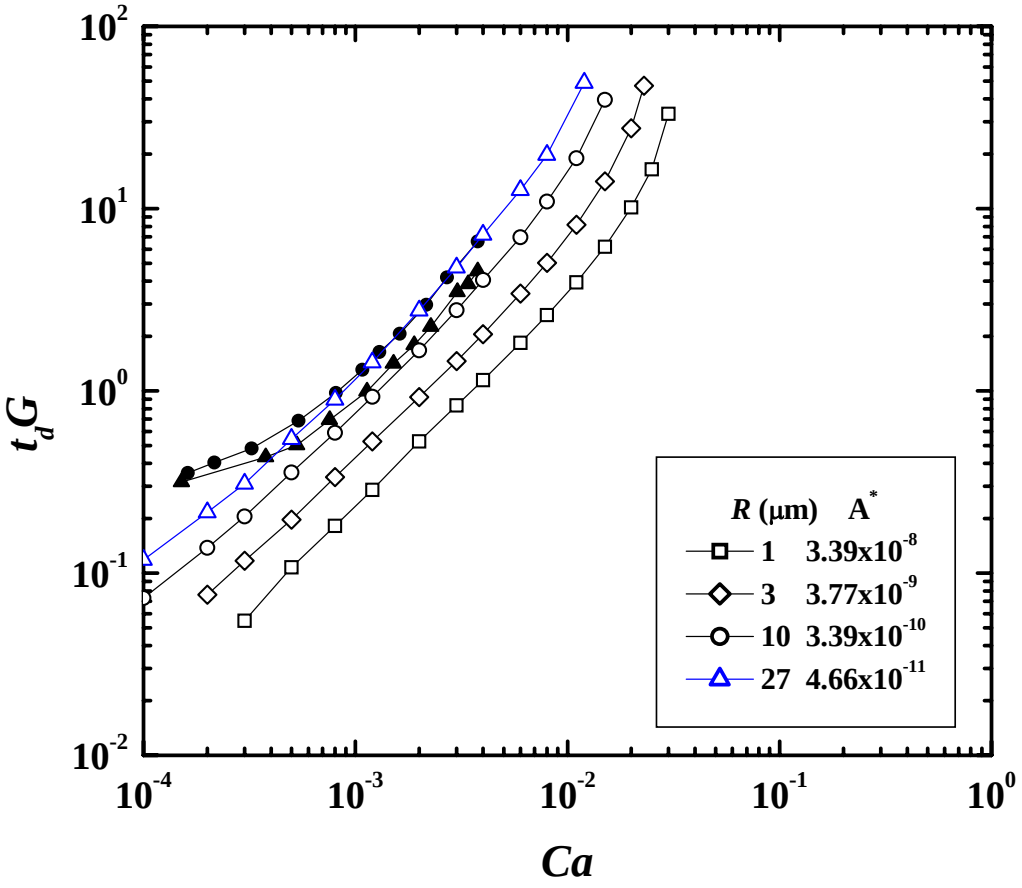

Figure 17. Drainage time as a function of *Ca* for various values of the dimensionless Hamaker constant at $\lambda = 6.8$. The experimental data are also presented by solid triangles for $R = 27.2$ μm and solid circles for $R = 39$ μm.

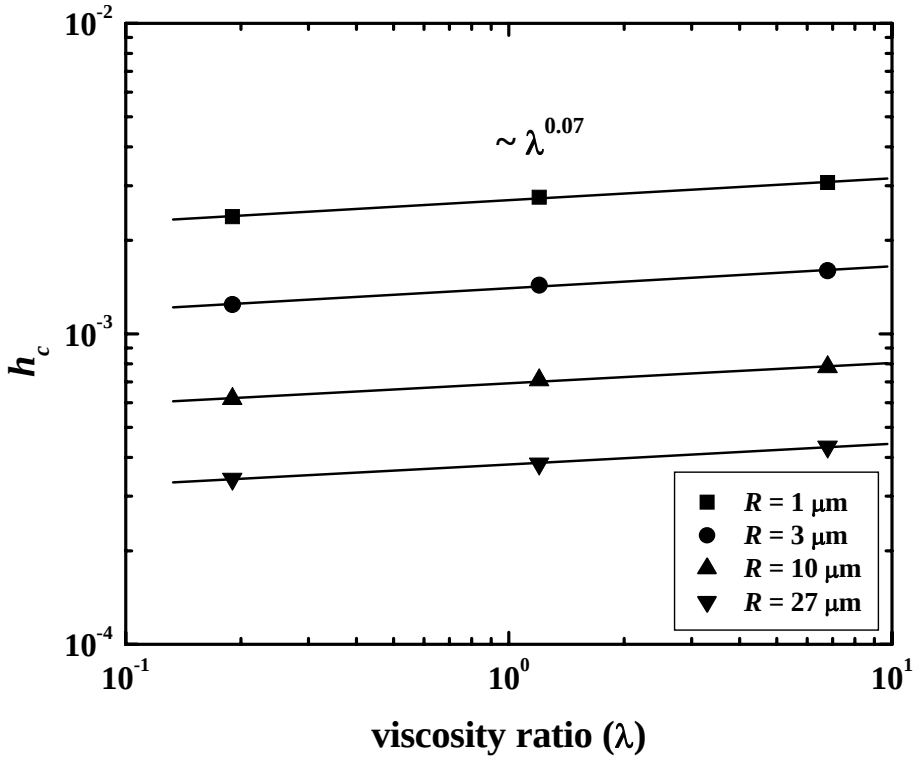

Figure 18. Critical film thickness for coalescence as a function of λ at $Ca = 0.008$.

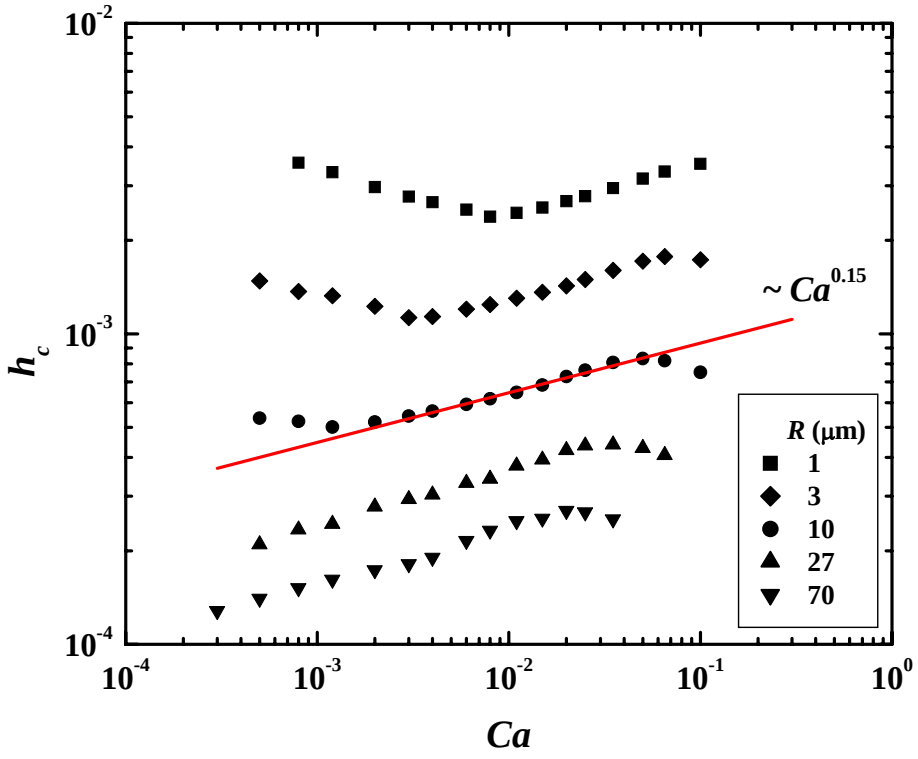

Figure 19. Critical film thickness for coalescence as a function of Ca for $\lambda = 0.19$.

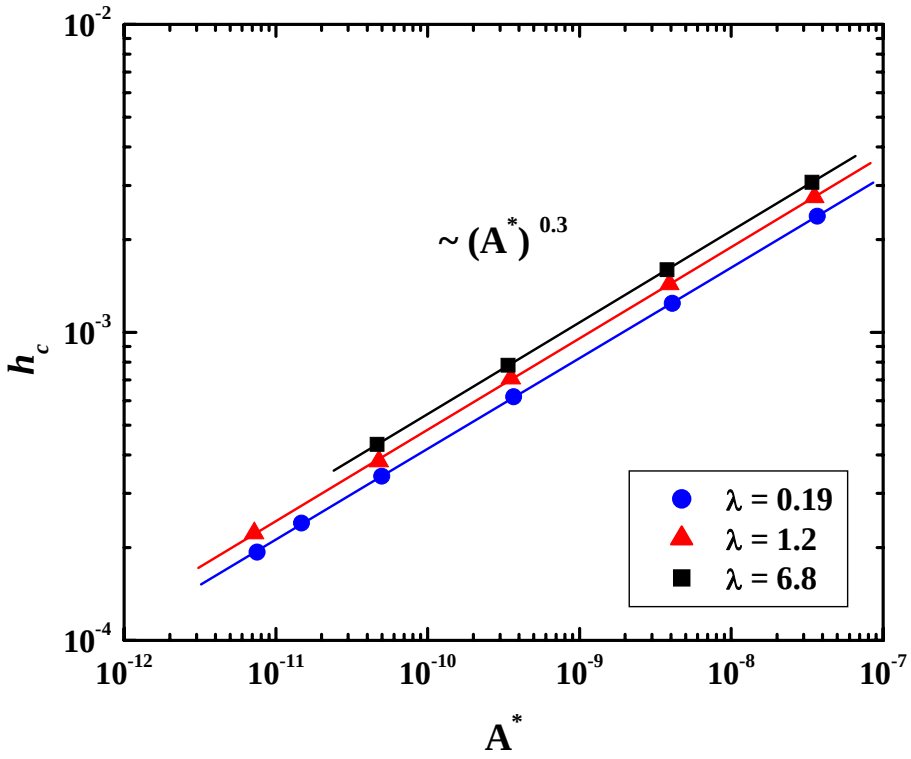

Figure 20. Critical film thickness for coalescence as a function of the dimensionless Hamaker constant.

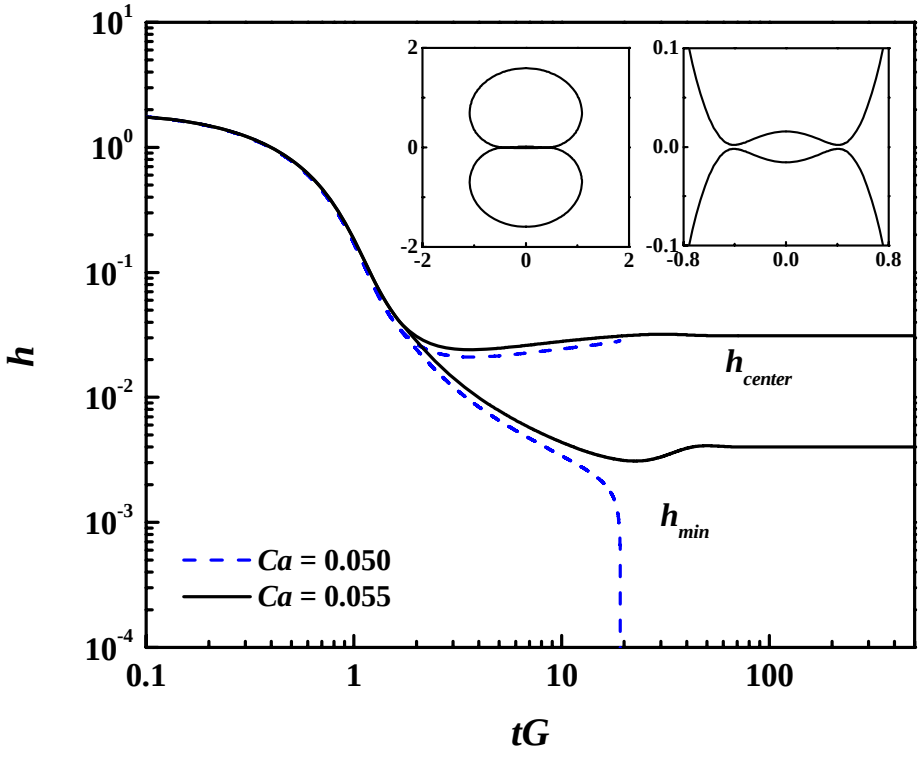

Figure 21. Evolution of the film shape for the two capillary numbers below and above the critical value at $A^* = 3.93\times10^{-9}$ and $\lambda = 1.2$. Insets show the stationary drop shape and the film profile for $Ca = 0.055$ at $tG = 100$.

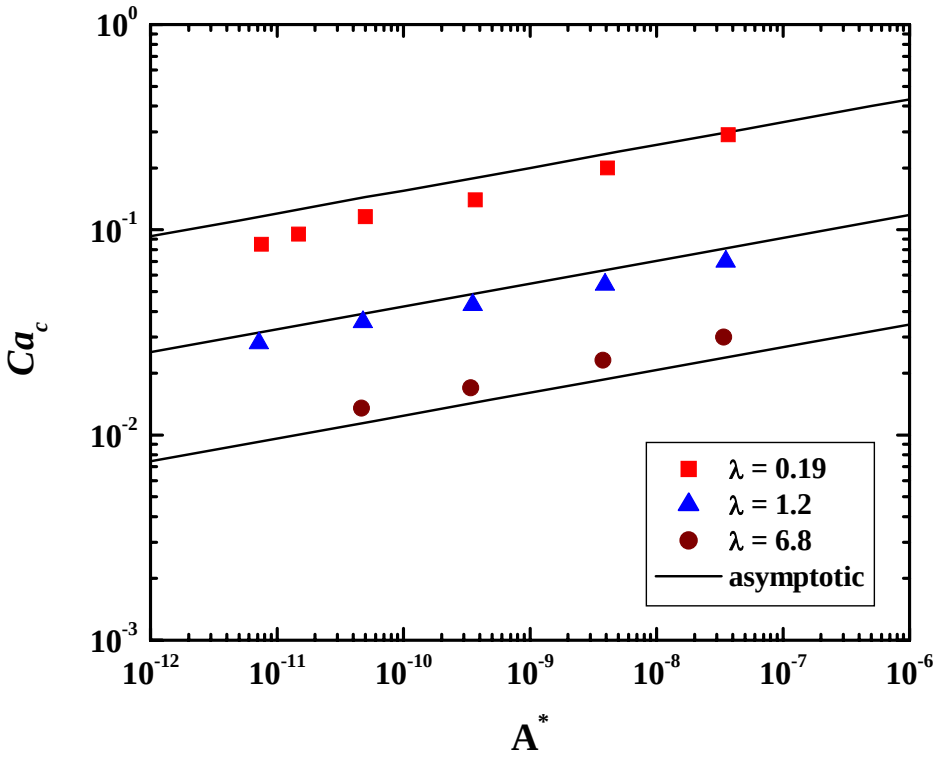

Figure 22. Critical capillary number for head-on collision as a function of the dimensionless Hamaker constant.

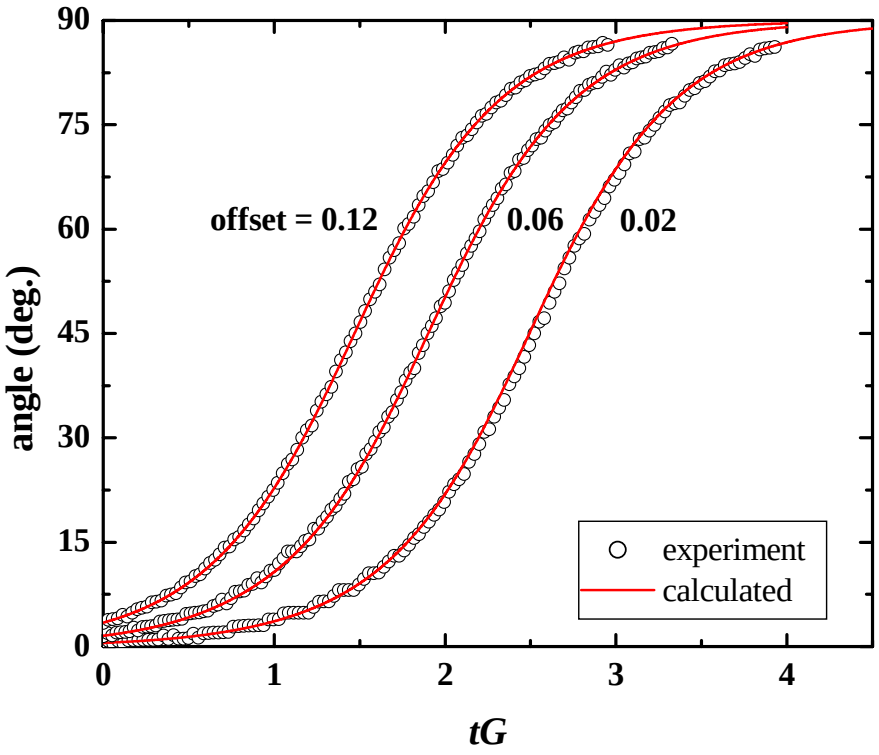

Figure 23. Comparison of typical experimental and theoretical trajectories for λ = 1.2. The capillary number is slightly higher than Ca_c (Ca = 0.00497 for offset = 0.02, Ca = 0.00433 for offset = 0.06, Ca = 0.00481 for offset = 0.12).

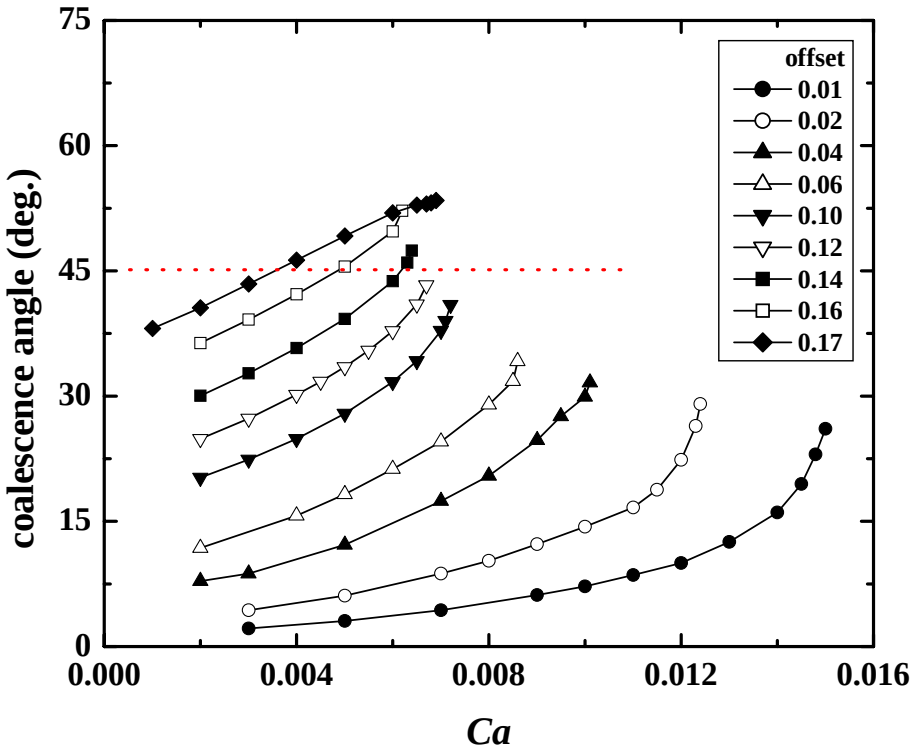

Figure 24. Coalescence angle as a function of Ca for collisions in a time-dependent flow at several initial offsets, $\lambda = 0.19$, and $A^* = 4.99\times10^{-11}$.

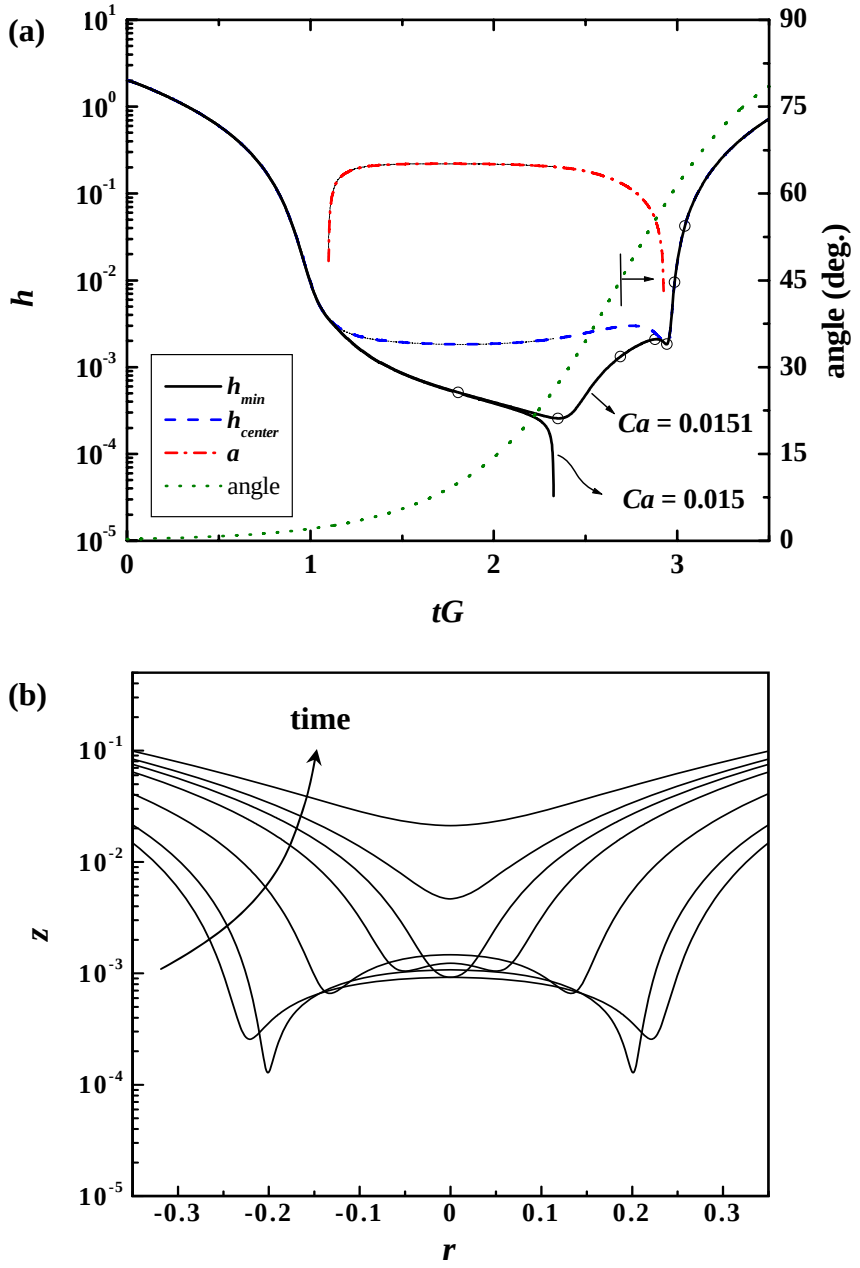

Figure 25. Evolution of the film shape for offset = 0.01, $\lambda = 0.19$ and $A^* = 4.99\times10^{-11}$: (a) $h_{\min}$, h_{center}, and the radius of the dimple, a, as a function of time; (b) thin film shapes at the moments indicated by open circles in figure(a) for $Ca = 0.0151$.

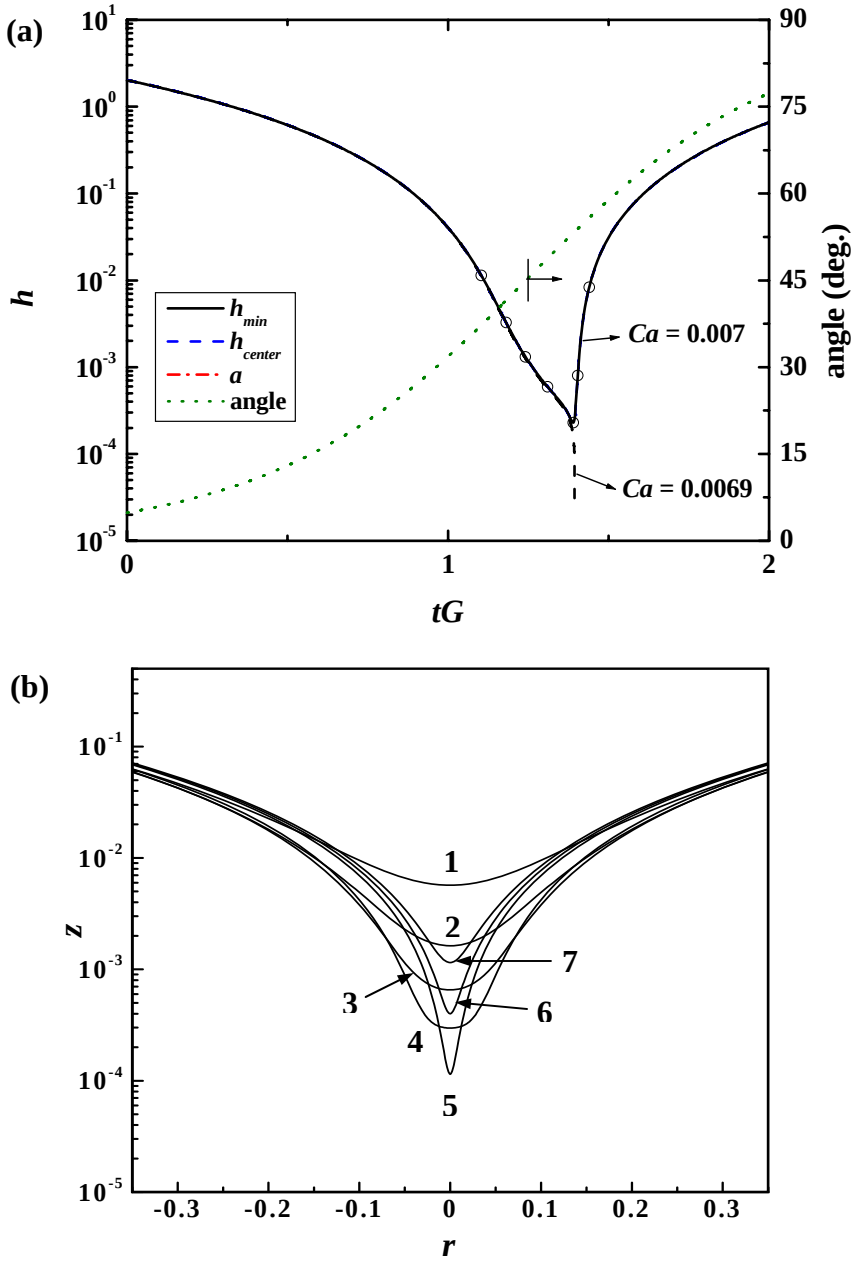

Figure 26. Evolution of the film shape for offset = 0.17, $\lambda = 0.19$ and $A^* = 4.99\times10^{-11}$: (a) $h_{\min}$, h_{center}, and the radius of the dimple, a, as a function of time; (b) thin film shapes at the moments indicated by open circles in figure(a) for $Ca = 0.007$.

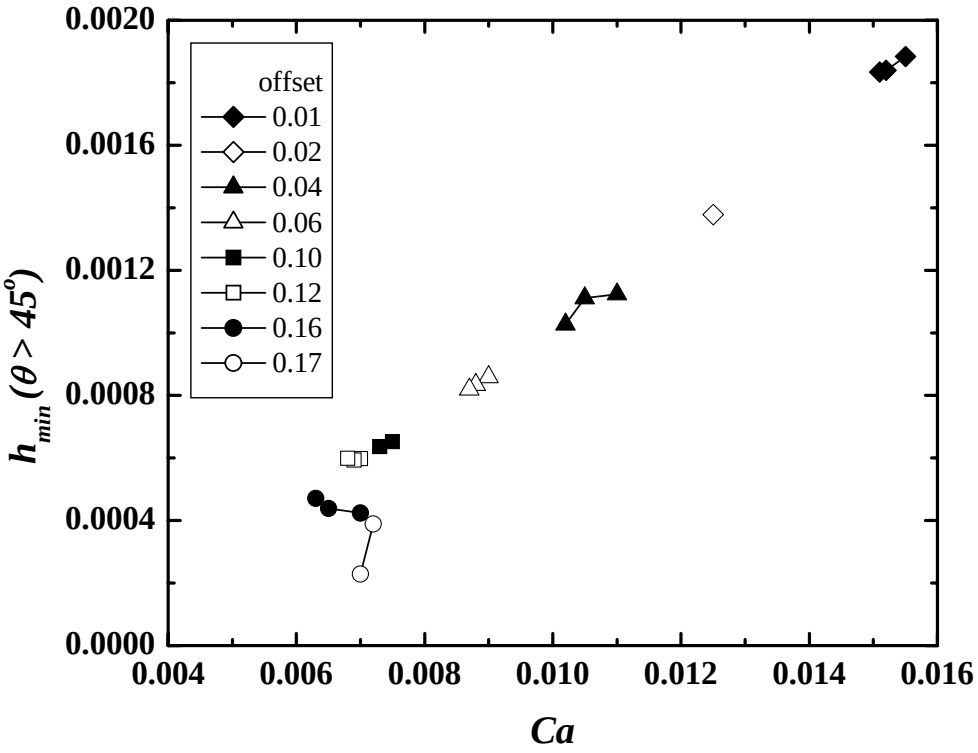

Figure 27. Secondary minimum of the film thickness for $\theta > 45^{\circ}$, when $Ca > Ca_c$ ($\lambda =$ 0.19).

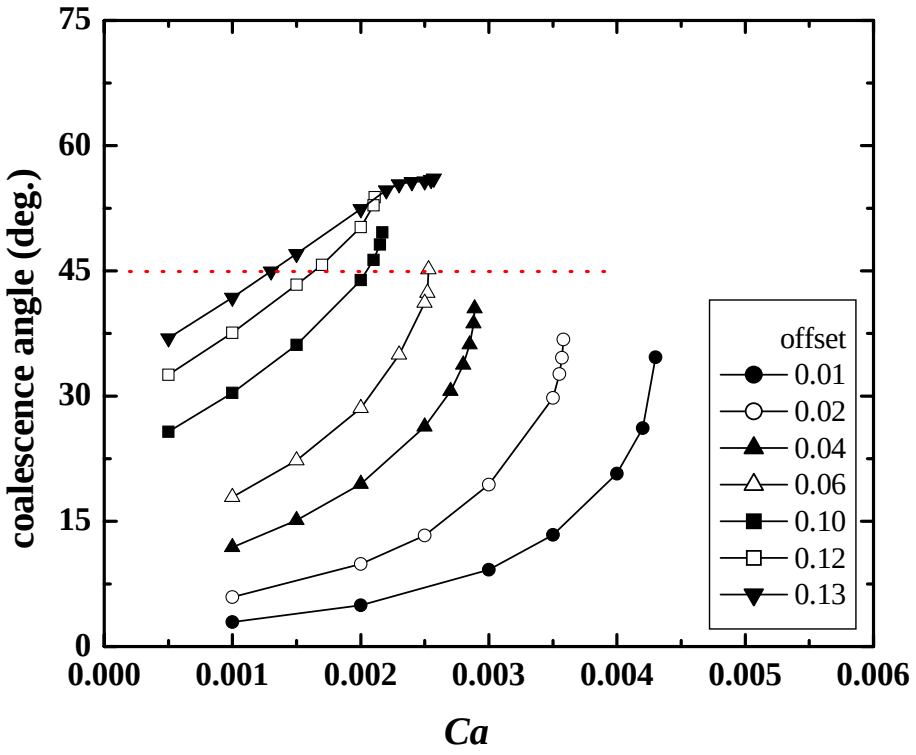

Figure 28. Coalescence angle as a function of Ca for collisions in a time-dependent flow at several initial offsets, $\lambda = 1.2$, and $A^* = 4.78\times10^{-11}$.

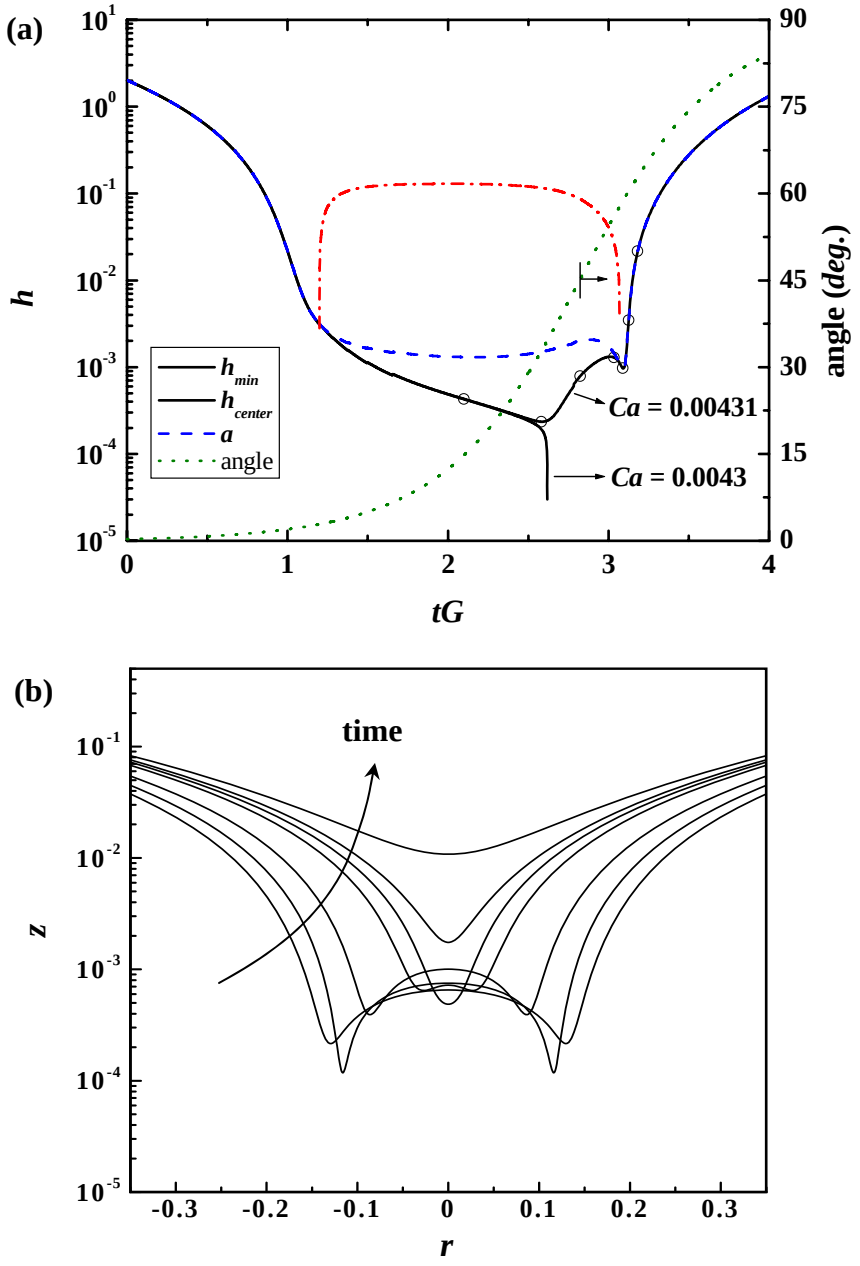

Figure 29. Evolution of the film shape for offset = 0.01, $\lambda = 1.2$ and $A^* = 4.78\times10^{-11}$: (a) $h_{\min}$, h_{center}, and the radius of the dimple, a, as a function of time; (b) thin film shapes at the points indicated by open circles in figure(a) for $Ca = 0.00431$.

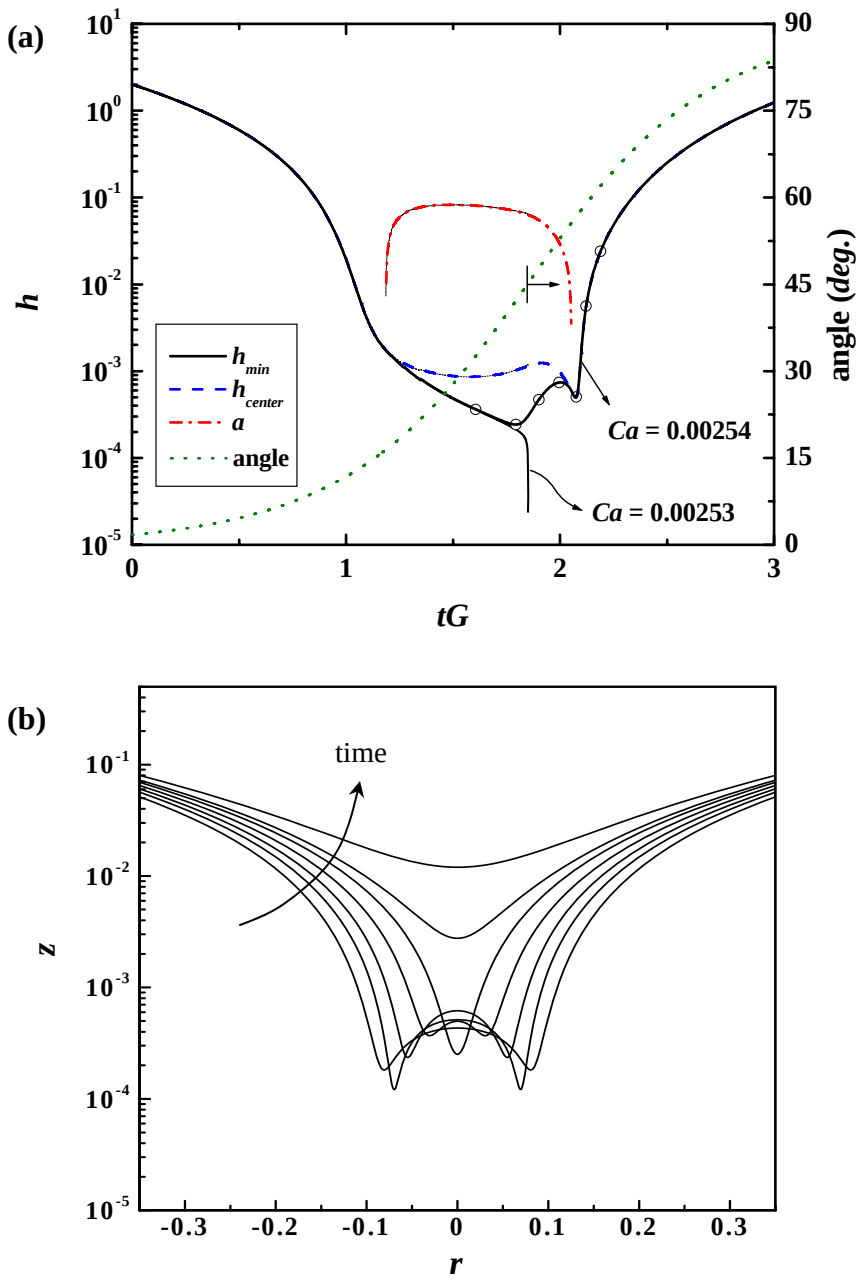

Figure 30. Evolution of the film shape for offset = 0.06, $\lambda = 1.2$ and $A^* = 4.78\times10^{-11}$: (a) $h_{\min}$, h_{center}, and the radius of the dimple, a, as a function of time; (b) thin film shapes at the points indicated by open circles in figure(a) for $Ca = 0.00254$.

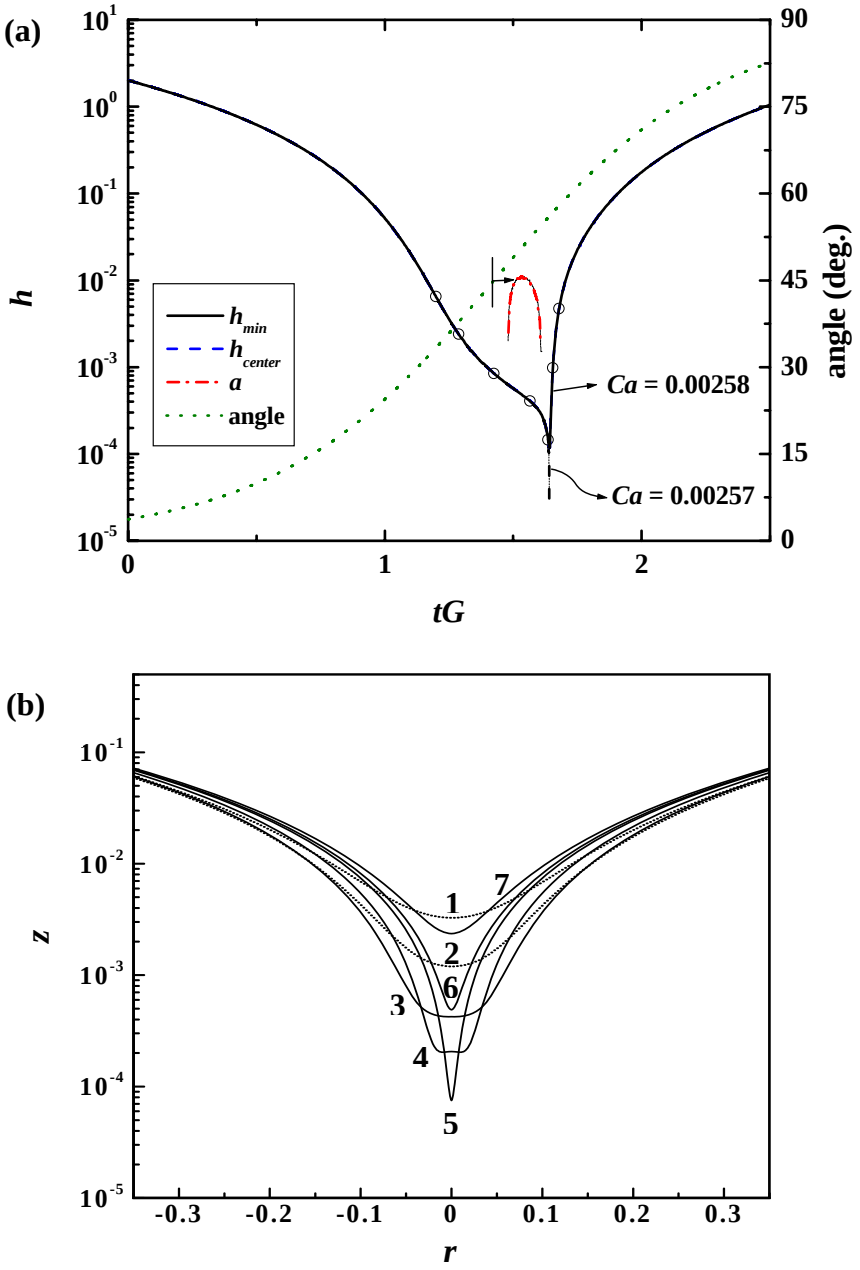

Figure 31. Evolution of the film shape for offset = 0.13, $\lambda = 1.2$ and $A^* = 4.78\times10^{-11}$: (a) $h_{\min}$, h_{center}, and the radius of the dimple, a, as a function of time; (b) thin film shapes at the points indicated by open circles in figure(a) for $Ca = 0.00258$.

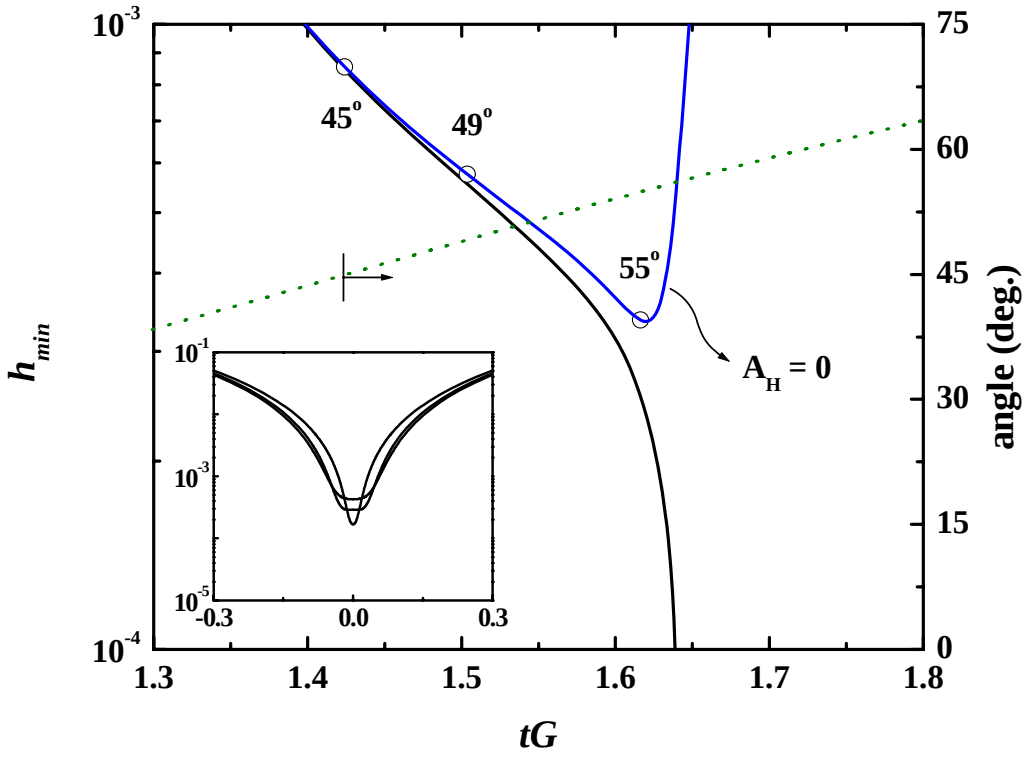

Figure 32. The comparison of the film evolutions with and without the van der Waals force for $Ca = 0.00253$. Inset shows the film shapes for $A_H = 0$ at the moments indicated in the figure.

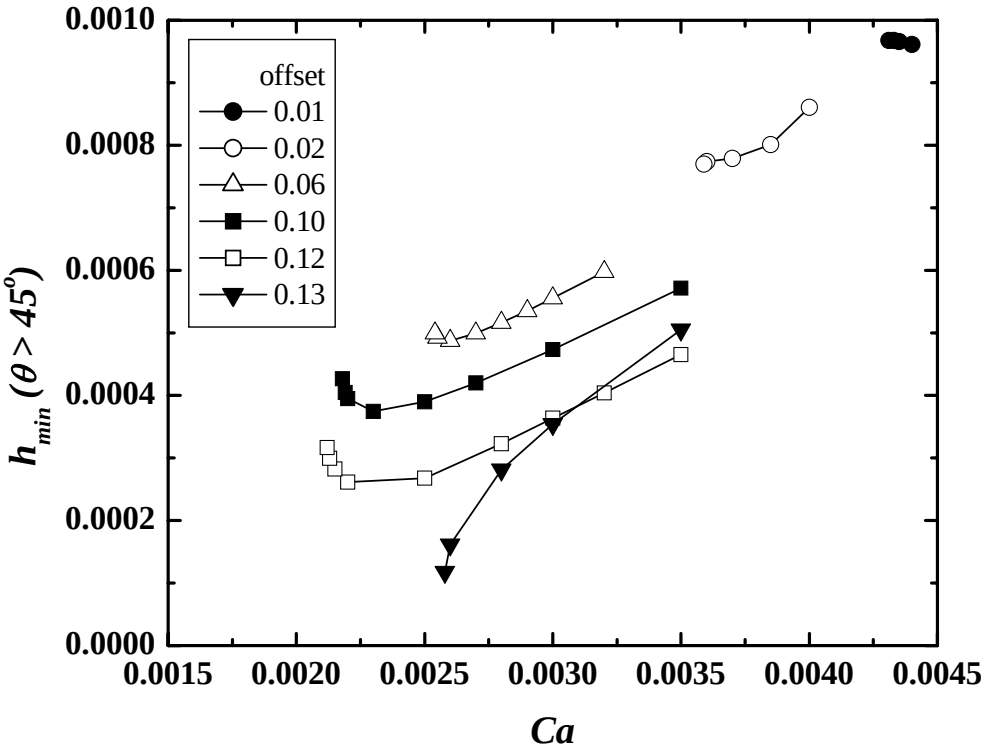

Figure 33. Secondary minimum of the film thickness for $\theta > 45^{\circ}$, when $Ca > Ca_c$ (λ = 1.2).

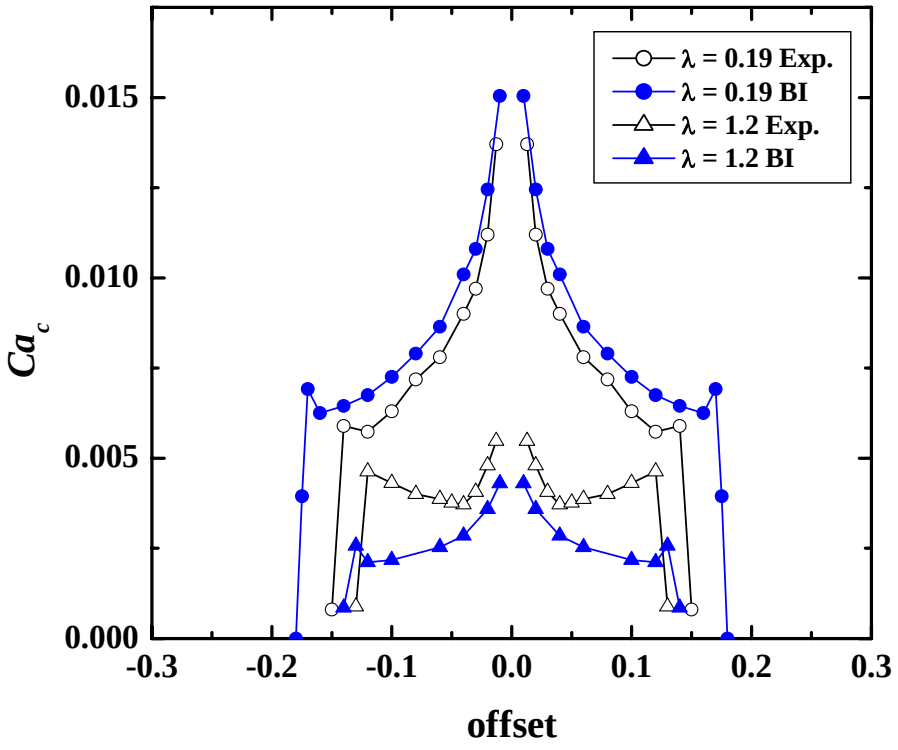

Figure 34. Critical capillary number as a function of the initial offset for the time-dependent flow simulation as well as the glancing collision experiment.